Geophysical Journal International

Geophys. J. Int. (2010) **183,** 339–357 doi: 10.1111/j.1365-246X.2010.04724.x

High-resolution lithospheric imaging with seismic interferometry

Elmer Ruigrok,[1] Xander Campman,[2] Deyan Draganov[1] and Kees Wapenaar[1]

[1] *Department of Geotechnology, Delft University of Technology, P.O. Box* 5048, 2600 *GA Delft, the Netherlands. E-mail: e.n.ruigrok@tudelft.nl*
[2] *Shell International Exploration and Production B.V., Rijswijk, The Netherlands*

Accepted 2010 July 6. Received 2010 June 30; in original form 2009 December 23

SUMMARY

In recent years, there has been an increase in the deployment of relatively dense arrays of seismic stations. The availability of spatially densely sampled global and regional seismic data has stimulated the adoption of industry-style imaging algorithms applied to converted- and scattered-wave energy from distant earthquakes, leading to relatively high-resolution images of the lower crust and upper mantle. We use seismic interferometry to extract reflection responses from the coda of transmitted energy from distant earthquakes. In theory, higher-resolution images can be obtained when migrating reflections obtained with seismic interferometry rather than with conversions, traditionally used in lithospheric imaging methods. Moreover, reflection data allow the straightforward application of algorithms previously developed in exploration seismology. In particular, the availability of reflection data allows us to extract from it a velocity model using standard multichannel data-processing methods. However, the success of our approach relies mainly on a favourable distribution of earthquakes. In this paper, we investigate how the quality of the reflection response obtained with interferometry is influenced by the distribution of earthquakes and the complexity of the transmitted wavefields. Our analysis shows that a reasonable reflection response could be extracted if (1) the array is approximately aligned with an active zone of earthquakes, (2) different phase responses are used to gather adequate angular illumination of the array and (3) the illumination directions are properly accounted for during processing. We illustrate our analysis using a synthetic data set with similar illumination and source-side reverberation characteristics as field data recorded during the 2000–2001 Laramie broad-band experiment. Finally, we apply our method to the Laramie data, retrieving reflection data. We extract a 2-D velocity model from the reflections and use this model to migrate the data. On the final reflectivity image, we observe a discontinuity in the reflections. We interpret this discontinuity as the Cheyenne Belt, a suture zone between Archean and Proterozoic terranes.

Key words: Image processing; Interferometry; Body waves; Crustal structure.

1 INTRODUCTION

A variety of seismic methods has been developed to image the lithosphere below an array of receivers using the body-wave responses from distant earthquakes. Particularly widely used are the receiver-function (RF) methods (Langston 1977; Wilson & Aster 2005), which image the *P*-*S* or *S*-*P* scattering potential. A higher resolution can be achieved when the complete forward-scattering potential is estimated (Bostock & Rondenay 1999), given that the source time functions (STF) of each earthquake can be estimated and deconvolved reliably (Bostock 2004). Free-surface-reflected phases (e.g. *Ppdp* or *Ppds*) may be added to further enhance the resolution, but model information is required to do this.

An attractive alternative is to migrate reflection responses obtained with seismic interferometry (SI). SI refers to the principle of generating seismic responses by crosscorrelating seismic observations at different receiver locations (Wapenaar *et al.* 2008; Schuster 2009). This technique is frequently used for the retrieval of surface waves between seismic receivers since the pioneering work by Campillo & Paul (2003), but can in principle be used to retrieve a complete Green's function, including the reflection response (Wapenaar 2004), dependent on the distribution of the actual sources. When a collection of reflection responses is obtained using SI, where a virtual source is retrieved at each station position, a reflectivity image can be constructed using standard seismic processing (Yilmaz & Doherty 2000) as was shown by Draganov *et al.* (2009) for an exploration-scale passive data set. A processing sequence that is similar to theirs could also be used for lithospheric imaging.

It was previously proposed by a number of researchers that SI may also be applied to transmission responses from distant earthquakes. Schuster *et al.* (2004) used only one synthetic phase response to

obtain a reflectivity image of a crustal model. Their approach is based on the theory of Claerbout (1968), who showed that the reflection response of a horizontally layered medium may be retrieved from the autocorrelation of the plane-wave transmission response. For actual earthquake data the results would not be satisfactory, because the subsurface is far more complicated than horizontally layered. Moreover, the STF and any scattering that is experienced by a phase before entering the lithosphere, would need to be perfectly deconvolved for. Nowack *et al.* (2006) showed a more elaborate imaging, but still with only one synthetic phase response in the Born approximation. Similar numerical tests, but with complete transmission responses of subsurface sources appeared in Draganov *et al.* (2006). In both numerical studies, only a few sources sufficed to make an image, given that the velocity model of the subsurface was known because the retrieved reflections themselves were too distorted to be used for estimating a model. Fan *et al.* (2006) described a combined reflection-retrieval and multiple-elimination scheme. Also their scheme is valid for horizontally layered media. Kumar & Bostock (2006) applied SI successfully on field data recorded by a single station at Hyderabad, India. Using exceptionally high-quality data, they retrieved a multicomponent, ray parameter-limited, reflection response for this single station. Tonegawa *et al.* (2009) retrieved waves between tiltmeter stations in the Tokai region, Japan. They made the assumption that the lithosphere below the station contains strong point diffractors, like in the ultrasonic experiment by Derode *et al.* (2003b). They first removed the deterministic part of the phase responses and subsequently only crosscorrelated the lithospheric coda to achieve an isotropic illumination. With their processing they retrieved primarily direct waves. Abe *et al.* (2007) applied SI, combined with an imaging step, on field data recorded by a dense array of receivers in central Japan. They showed that the resulting image has a higher resolution than the image obtained from RF. They used phase responses from 10 earthquakes from varying azimuths. This might have sufficed to obtain a reliable image, though the work from Draganov *et al.* (2006) suggests that, for an approximately layered medium, this is insufficient for obtaining reliable reflection responses.

Despite a few imaging successes with the help of SI, the question remained whether, with SI, a true multidimensional lithospheric reflection response can be obtained under realistic conditions. The realistic conditions of concern are an irregular distribution of earthquakes, different phase-responses that overlap in time and a lithosphere that is unlikely to contain a large number of point scatterers. To address the applicability of SI under these conditions, we generate synthetic data with similar source-side reverberations (SSR) and illumination characteristics like a field data set from the Laramie broad-band array (2000–2001). We evaluate sampling requirements and introduce SI adaptations for irregular source distributions. Artefacts are to be expected, caused by both an irregular illumination and by SSR. Subsequently, we study with which SI adaptation these artefacts can be suppressed most successfully. After ascertaining the reliability of the retrieved reflections, we use them to estimate a 2-D *P*-wave velocity model of the lithosphere. Finally, the imaging accuracy is shown by stacking and migrating the obtained reflection responses, for both the synthetic and field data.

2 SEISMIC INTERFEROMETRY

We apply SI to *P*-wave phases caused by distant earthquakes and their *P*-wave scattering near an array of receivers. Fig. 1(a) depicts the different *P*-wave phases that we consider. In particular, we use the direct transmissions *P* and *PKP*, since they are the first to arrive and are, consequently, not disturbed by coda from earlier phases. In Wapenaar & Fokkema (2006) an acoustic 3-D SI relation is derived for a configuration with receivers on a free surface and illumination from below. This SI relation consists of correlations of receivers at the surface, followed by an integration of correlations over source positions in the subsurface. In Appendix A we estimate what the minimum (in-plane) source sampling for this integral needs to be for a lithospheric application and show that the maximum allowed spacing between large earthquakes is about 1000 km. There are many places on the Earth where this source density is not reached. Fortunately, the required source spacing can be reached when a

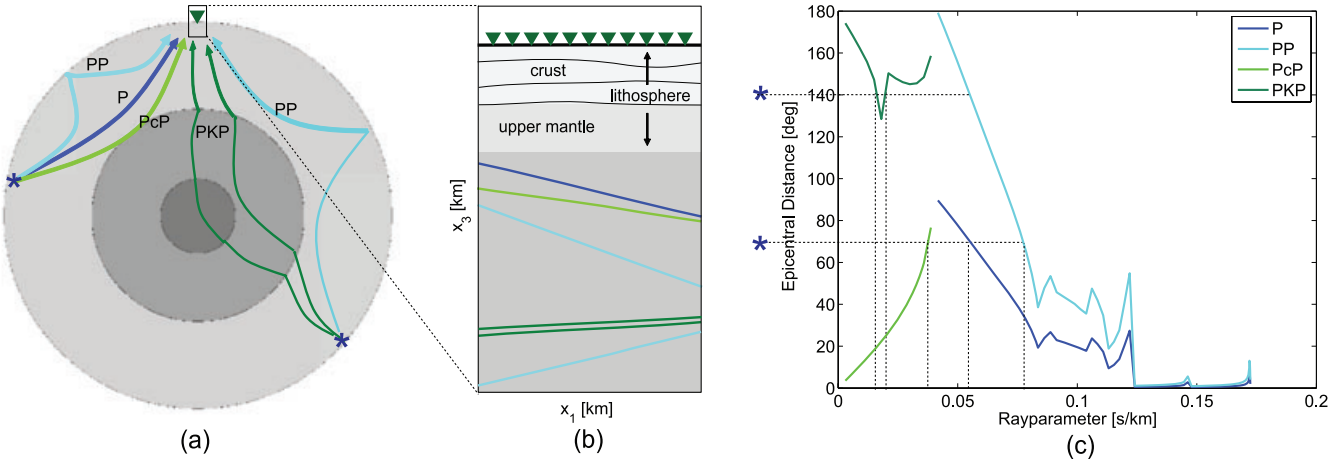

Figure 1. (a) A depiction of the ray paths for different *P*-wave phases between two earthquake sources (stars) and a regional array of receivers (triangle). For the teleseismic source (left-hand panel) *P*, *PP* and *PcP* are shown while for the global source (right-hand panel) *PKP* and its branch through the inner core (*PKIKP*) are shown. (b) An enlargement of the subsurface below the array with the wave fronts of the different phases (coloured dipping lines) travelling upwards, just before they hit the lithosphere from below. The lateral (x_1) and depth axis (x_3) have equal scaling. The wave fronts are depicted with only half the dip of what may be expected. In reality, the different phases arrive near the array with a considerable time lapse. (c) The different phases as a function of epicentral distance (Δ) and absolute ray parameter $|p|$ for which they exist (Knapmeyer 2004). From this graph can be read, the $|p|$ of the phases caused by the teleseismic source ($\Delta = 70^\circ$) and the global source ($\Delta = 140^\circ$).

3-D distribution of point sources may be represented by a 2-D distribution of sources, in-plane with the receiver array. This will be shown in the following.

For distant earthquakes, the distance is much larger than the length of the array of receivers and, consequently, an incoming wave caused by a distant earthquake is by approximation a plane wave when it reaches the lithosphere. In Fig. 1(b) the planar wave fronts of the different phases are depicted as they travel upwards through the mantle and just before they hit upon the heterogeneous lithosphere below the array. Thus, near the array, each global and teleseismic phase may be treated as a separate effective plane wave, characterized by a single horizontal ray parameter p. The SI relation from Wapenaar & Fokkema (2006) is written as an integration over point sources $\mathbf{x}$. In the following we will rewrite their relation to an integration over plane-wave sources expressed in p.

As a first step, we present a 2-D approximation of the relation in Wapenaar & Fokkema (2006).

$$\int_{\partial\mathbb{S}_1} G(\mathbf{x}_\mathcal{A}, \mathbf{x}, -t) * G(\mathbf{x}_\mathcal{B}, \mathbf{x}, t)\mathrm{d}\mathbf{x} \propto G(\mathbf{x}_\mathcal{B}, \mathbf{x}_\mathcal{A}, -t) + G(\mathbf{x}_\mathcal{B}, \mathbf{x}_\mathcal{A}, t), \quad (1)$$

where $G(\mathbf{x}_\mathcal{A}, \mathbf{x}, t)$ denotes the Green's function observed at location $\mathbf{x}_\mathcal{A}$ (one of the receivers) due to a source at $\mathbf{x}$, $*$ denotes convolution and where a proportionality sign is used since we have left out all the amplitude terms.

As a second step, we change the variables of integration from Cartesian (x_1, x_3) to polar coordinates (r, ϕ).

$$\int_{\partial\mathbb{S}_1} G(\mathbf{x}_\mathcal{A}, \mathbf{x}, -t) * G(\mathbf{x}_\mathcal{B}, \mathbf{x}, t) r\,\mathrm{d}\phi \propto G(\mathbf{x}_\mathcal{B}, \mathbf{x}_\mathcal{A}, -t) + G(\mathbf{x}_\mathcal{B}, \mathbf{x}_\mathcal{A}, t), \quad (2)$$

where $\mathbf{x} = (r, \phi)$ on $\partial\mathbb{S}_1$, with r being the radius and ϕ the angle. $\partial\mathbb{S}_1$ is the surface (or actually a curved line in 2-D) containing the sources. Together with the free surface it should ideally form a closed surface. The retrieved response $G(\mathbf{x}_\mathcal{B}, \mathbf{x}_\mathcal{A}, t)$ contains the reflection response between the two receiver positions (triangles in Fig. 1). To retrieve a response between one virtual source $\mathbf{x}_\mathcal{A}$ and several receivers, eq. (2) would need to be repeated for varying $\mathbf{x}_\mathcal{B}$. Since a loss-less medium is assumed for eq. (2), the phase responses would need to be corrected for losses before crosscorrelation. In Draganov *et al.* (2010) a procedure is described to estimate an average quality factor Q with SI. This Q, in turn, may be used to estimate an amplitude correction term, to be applied to the data prior to crosscorrelation. We expect only small losses in the lithosphere. For small and moderate losses a correction may be left out (Ruigrok *et al.* 2009).

As a third step, we change the coordinate of integration in eq. (2) from ϕ to p (Appendix A), yielding

$$\int G(\mathbf{x}_\mathcal{A}, p, -t) * G(\mathbf{x}_\mathcal{B}, p, t) \frac{r v_p}{\sqrt{1 - v_p^2 p^2}}\mathrm{d}p \propto G(\mathbf{x}_\mathcal{B}, \mathbf{x}_\mathcal{A}, -t) + G(\mathbf{x}_\mathcal{B}, \mathbf{x}_\mathcal{A}, t), \quad (3)$$

where $G(\mathbf{x}_\mathcal{B}, p, t)$ is the phase response of a plane wave with ray parameter p measured at $\mathbf{x}_\mathcal{B}$. The term $\frac{r v_p}{\sqrt{1-v_p^2 p^2}}$ weighs the contributions from different sources. Since v_p (velocity just below the lithosphere) is similar for different sources, the weighing term is only smoothly varying in p and does therefore not alter the phase of the retrieved Green's function. On that account, we also neglect this amplitude term, reducing eq. (3) to

$$\int G(\mathbf{x}_\mathcal{A}, p, -t) * G(\mathbf{x}_\mathcal{B}, p, t)\mathrm{d}p \propto G(\mathbf{x}_\mathcal{B}, \mathbf{x}_\mathcal{A}, -t) + G(\mathbf{x}_\mathcal{B}, \mathbf{x}_\mathcal{A}, t). \quad (4)$$

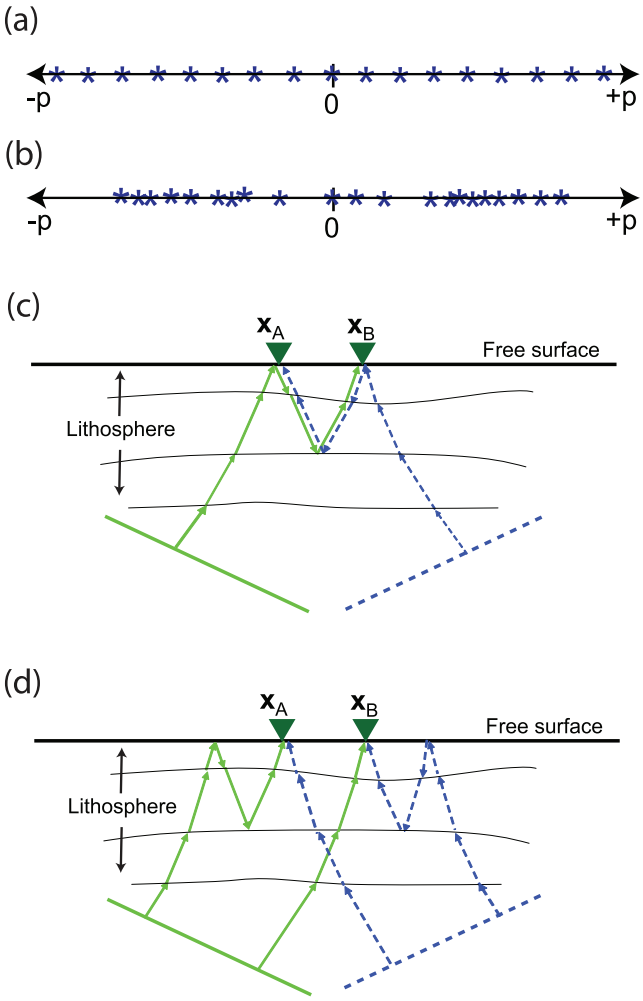

Figure 2. In (a) an ideal illumination is shown for plane-wave sources, expressed in ray parameters. In (b) a more realistic distribution of plane-wave sources is shown. In (c) and (d) examples of ray paths are indicated that in (c) do contribute to the retrieval of a reflection after crosscorrelation, but in (d) do not.

Fig. 2(a) shows an ideal illumination from plane-wave sources (represented by stars) with which the complete response between $\mathbf{x}_\mathcal{A}$ and $\mathbf{x}_\mathcal{B}$ would be retrieved when eq. (4) is implemented. The illumination is ideal when phase responses are available in a well-sampled range, $p = [0, \pm 1/v_p^{ns}]$ (Fig. 2a), where v_p^{ns} is the near-surface velocity. Fig. 2(b) depicts a more realistic illumination, with missing illumination at large ray parameters and an irregular illumination at small ray parameters. Large ray parameters correspond to body-wave phases from nearby sources of which the wavefields are not planar and for which different triplications cannot easily be separated and aligned. Omitting large ray parameters means that guided waves and body waves at large offsets would not be retrieved. Small ray parameters correspond to body-wave phases from distant sources with well-defined planar wavefields emerging on the lithosphere. By using illumination with small ray parameters, body waves at near and intermediate offsets can be retrieved, which are the most relevant ones for obtaining a reflectivity image.

Using only *P* phases from teleseismic distances would not be sufficient, since their illumination is limited between ray parameters of $[-0.08, -0.04]$ and $[0.04, 0.08]$ s km^{-1} (Fig. 1c). *PKP* phases are used to fill the gap of the very small ray parameters, while *PP* and *PcP* are used to enhance the sampling. The irregular illumination stems from the irregular distribution of earthquakes and the heterogeneous nature of the Earth. The influence of this irregularity is studied in Section 4.

With eq. (4) both a causal and an acausal response are retrieved. This is explained in Fig. 2(c) for a single reflection. The reflection drawn between $\mathbf{x}_\mathcal{A}$ and $\mathbf{x}_\mathcal{B}$ can be retrieved at positive times by contributions from sources with positive p contributing to the Fresnel zone around the solid ray. The same reflection can be retrieved at negative times by contributions from sources with negative p contributing to the Fresnel zone around the dashed ray. The above reasoning holds for an approximately layered medium. For a complex medium, a phase with a negative ray parameter may still give contributions to $G(\mathbf{x}_\mathcal{B}, \mathbf{x}_\mathcal{A}, t)$, for example, by scattering from point diffractors. The standard procedure would be to add the time-reversed acausal result of eq. (4) to the causal result, to increase the effective sampling. Alternatively, the contributions from the negative ray parameters can be time-reversed prior to integration. If $[p^-_{\min}, p^-_{\max}]$ and $[p^+_{\min}, p^+_{\max}]$ are the ray parameter bands in which we have illumination, the discretized version of eq. (4) can be split up in a sum over positive and negative ray parameters:

$$\sum_{p^-_{\min}}^{p^-_{\max}} I(\mathbf{x}_\mathcal{A}, \mathbf{x}_\mathcal{B}, p, t)\Delta p \propto G(\mathbf{x}_\mathcal{B}, \mathbf{x}_\mathcal{A}, -t) + N^-(t) \tag{5}$$

and

$$\sum_{p^+_{\min}}^{p^+_{\max}} I(\mathbf{x}_\mathcal{A}, \mathbf{x}_\mathcal{B}, p, t)\Delta p \propto G(\mathbf{x}_\mathcal{B}, \mathbf{x}_\mathcal{A}, t) + N^+(t), \tag{6}$$

where $I(\mathbf{x}_\mathcal{A}, \mathbf{x}_\mathcal{B}, p, t)$ stands for the integrand of eq. (4). $N^-(t)$ and $N^+(t)$ contain correlations of non-specular rays, with negative and positive ray parameter, respectively. These are correlations of waves with non-overlapping raypaths (Fig. 2d). For an approximately 1-D medium $N^\pm(t)$ would be zero if the sums (eqs 5 and 6) cover the complete ray parameter band and satisfy the sampling condition for integral eq. (4). For a strongly heterogeneous medium eqs (5) and (6) would need to be summed to remove the noise terms. In practice, $N^\pm(t)$ contains remnants of the non-specular correlations, that have not cancelled completely in the summation process. These remnants are called correlation noise. By adding the time reversed of eq. (5) to eq. (6),

$$\sum_{p^-_{\min}}^{p^-_{\max}} I(\mathbf{x}_\mathcal{A}, \mathbf{x}_\mathcal{B}, p, -t)\Delta p + \sum_{p^+_{\min}}^{p^+_{\max}} I(\mathbf{x}_\mathcal{A}, \mathbf{x}_\mathcal{B}, p, t)\Delta p \propto 2G(\mathbf{x}_\mathcal{B}, \mathbf{x}_\mathcal{A}, t) + N^-(-t) + N^+(t), \tag{7}$$

the effective sampling is increased while a part of the correlation noise is isolated at negative times. Thus, by rejecting the negative times, the signal-to-noise ratio is increased. In the following we will call this the time reversal before integration (TRBI) approach. There is no need for applying TRBI when a well-sampled source distribution is available. For a strongly heterogenous subsurface it would even be disadvantageous to apply TRBI, because it would lead to additional noise that would otherwise (with eq. 4) be cancelled.

By using a limited ray parameter band, also the retrieved Green's function in eq. (7) will be ray parameter limited. As a consequence, the slope of a primary reflection is incorrectly retrieved beyond a maximum half-offset $h_{\max}(t)$. Assuming a well-sampled illumination band $[0, p_{\max}]$, a 1-D velocity model with an average velocity $\tilde{v}_p(t)$ and an infinite frequency, $h_{\max}$ may be expressed as

$$h_{\max}(t) = \frac{p_{\max} t \{\tilde{v}_p(t)\}^2}{2\sqrt{1 - \{\tilde{v}_p(t)\}^2 p^2_{\max}}}, \tag{8}$$

where t is the two-way traveltime.

To retrieve a reflection correctly for a finite frequency, a Fresnel zone around the stationary point needs to be sampled (Schuster *et al.* 2004; Snieder 2004). Therefore, in practice, $h_{\max}(t)$ will be smaller than estimated in eq. (8).

The moment tensor of an earthquake is of little relevance for this application of SI. Since the size of a typical array of receivers ($<10^2$ km) is at least one order of magnitude smaller than the distances to the sources ($>10^3$ km), it may be assumed that the entire array lies within one focal plane. In this case, the observed responses at $\mathbf{x}_\mathcal{A}$ and $\mathbf{x}_\mathcal{B}$ in eq. (4) may be written as a convolution of only the STF with the Green's functions $G(\mathbf{x}_\mathcal{A}, p, t)$ and $G(\mathbf{x}_\mathcal{B}, p, t)$. In principle, it would be better to remove the STFs prior to integration. Regrettably, it is notoriously hard to estimate the STFs reliably and to deconvolve them in a stable manner (Kumar & Bostock 2006). This is especially so for the relative low-magnitude earthquakes recorded by a portable array, as in our case. In our experience, suppressing the sidelobes of the autocorrelated STFs in the integration process gives better results than removing the STFs prior to integration. By assigning an STF to the observed Green's functions in eq. (4), the retrieved response will be a convolution of the Green's function between $\mathbf{x}_\mathcal{A}$ and $\mathbf{x}_\mathcal{B}$ with a stack of autocorrelations of all individual STFs. Through the autocorrelation, the STFs become all zero-phase, which facilitates a successful integration, even when the earthquake responses have very different—and very complicated—STFs.

3 LARAMIE ARRAY

We apply the above theory to earthquake responses recorded by the Laramie array. The array was installed near the town of Laramie, in Wyoming, USA and hence the name. It was deployed between 2000 October and 2001 May to study the Archean–Proterozoic Cheyenne Belt suture (Dueker & Zurek 2001). The array consists of 31 three-component broad-band receivers, as depicted in Fig. 3(a), with an average spacing of 2.6 km. The orientation of the array is favourable, approximately in-plane with a large part of the Ring of Fire (Fig. 3c). The data was previously processed to obtain RF images (Hansen & Dueker 2009).

In eq. (4), the integration is over plane waves radiated by sources in the vertical plane. For finite frequency, the source locations may be located outside this plane, as long as their contributions to the integral are in phase with the contribution from sources in the plane. Fig. 3(b) depicts the size of the region of source locations that would contribute in phase. This region is computed in Appendix B. From all the recorded earthquake responses, only those are selected that are from sources within the coloured zone in Fig. 3(b) and with a magnitude larger than 5. All the selected three-component responses are bandpass filtered between 0.3 and 1.5 Hz, rotated and decomposed to *P*, *SV* and *SH* components as further explained in Appendix C. Using only the *P* component, time windows of 100 s are chosen to isolate *P*, *PP*, *PcP* and *PKP* arrivals and their reverberations, where possible. Subsequently, timing errors between the different receivers and statics are removed by aligning on the direct arrival with an iterative crosscorrelation scheme. Each trace in a phase response is normalized with the maximum amplitude of the

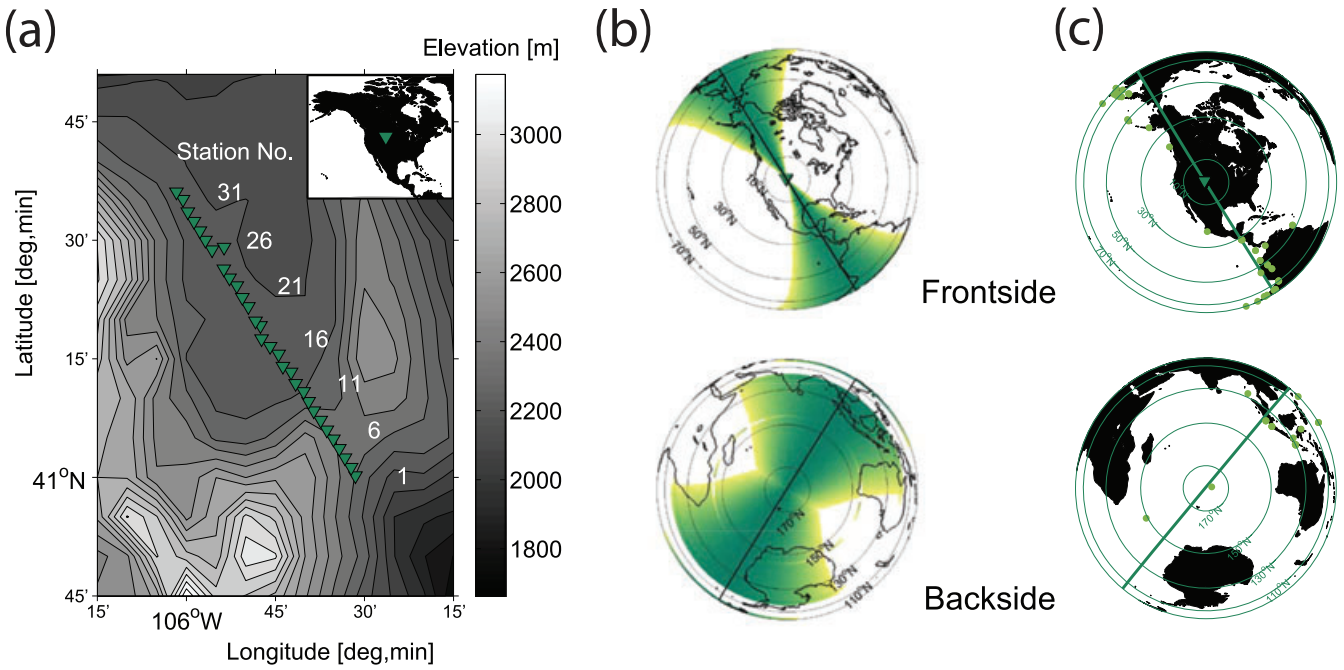

Figure 3. (a) The Laramie array of seismic receivers (triangles) and the local topography (shading). (b) Approximation of the first Fresnel zone for the *P* and *PKP* phase, for epicentral distances $\Delta = [0, 90^\circ]$ (up) and $\Delta = [90, 180^\circ]$ (down), for an offset equal to or smaller than 40 km. (c) The distribution of earthquakes of which the responses are processed for $\Delta = [0, 90^\circ]$ (up) and $\Delta = [90, 180^\circ]$ (down). In (b) and (c) the concentric circles depict the epicentral distance with respect to the Laramie array. The straight line is the extended great circle through the array, which has an average orientation of 328°.

direct arrival, to correct for differences in near-surface amplifications. An implicit assumption in relation (4) is that the plane waves have equal energy. Since this assumption is not fulfilled for natural sources, as a last step, we normalize the energy in each phase response. From 39 earthquake responses 69 separate phase responses are extracted.

Despite the fact that only events in the first Fresnel zone are selected, the average illumination is still not in-plane with the array (Fig. 3c). The azimuthal illumination bias, which leads to small kinematic errors in the retrieved response, is suppressed through the following azimuthal correction. We define p^{src} as the horizontal ray parameter connecting the source and the receiver through a homogeneous background model and $p^{1,\mathrm{src}}$ as its projection on the array vector. Thus $p^{1,\mathrm{src}} = p^{\mathrm{src}} \cos(\theta)$, where the source-to-array azimuth θ is defined as the angle between the array orientation (a best fitting great circle through the stations) and a great circle through the source and the middle station. After aligning a response on the direct wave, the move-out is restored with traveltime differences computed with p^{src} instead of $p^{1,\mathrm{src}}$. Hence, the direct wave obtains a move-out as if the source location was in-plane with the array. This azimuthal correction is justified if the array is small with respect to the distance to a source and if the medium may be approximated to be laterally invariant within the coloured zone in Fig. 3(b).

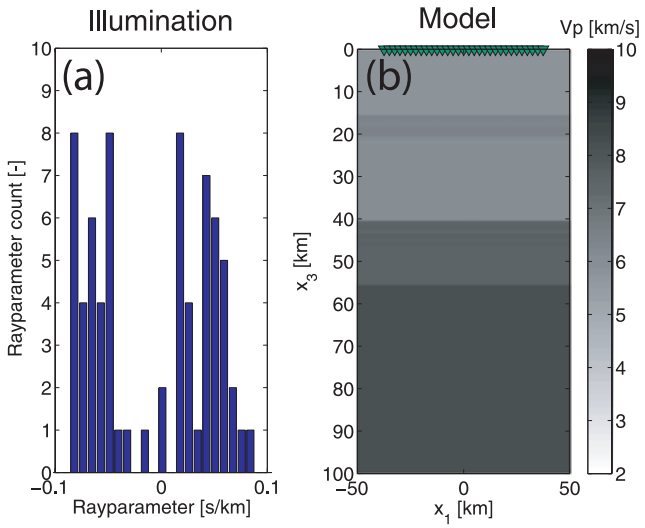

Figure 4. (a) A histogram distribution of the ray parameters of the selected phase responses. A bin size $dp = 0.0083\ \mathrm{s\,km^{-1}}$ is taken, which corresponds to the required sampling of eq. (4). (b) A simplified *P*-wave velocity model (v_p) for the crust and upper mantle, with 31 receivers (triangles) on the free surface.

4 COMPARISON OF SI APPROACHES

The p-distribution of the 69 effective sources is depicted in Fig. 4(a). Clearly, the integral in eq. (4) is sampled strongly irregularly. Ray parameters from *P* phases at teleseismic distances are overrepresented, whereas small ray parameters are underrepresented. To find a good approach to deal with the irregularity, we model a 2-D synthetic data set with the same irregular ray parameter distribution and receiver geometry as the actual data set. We use a simplified lithospheric model (Fig. 4b) based on the findings of Chulick & Mooney (2002) from a nearby refraction survey. The main feature is the Moho at 40 km depth, separating a crystalline crust ($v_p = 6.0\ \mathrm{km\,s^{-1}}$, $\rho = 2730\ \mathrm{kg\,m^{-3}}$) from the upper mantel ($v_p = 7.6\ \mathrm{km\,s^{-1}}$, $\rho = 3310\ \mathrm{kg\,m^{-3}}$). Subsequently, we apply SI to the 69 transmission responses, to retrieve the response as if there was a source at station 16 and receivers at all other station positions. To suppress edge effects, the edges of the integrand (in eqs 4 and 7) are tapered. In Fig. 5(a) one of the 69 synthetic transmission responses is shown. In Figs 5(b)–(d) different approaches are tested

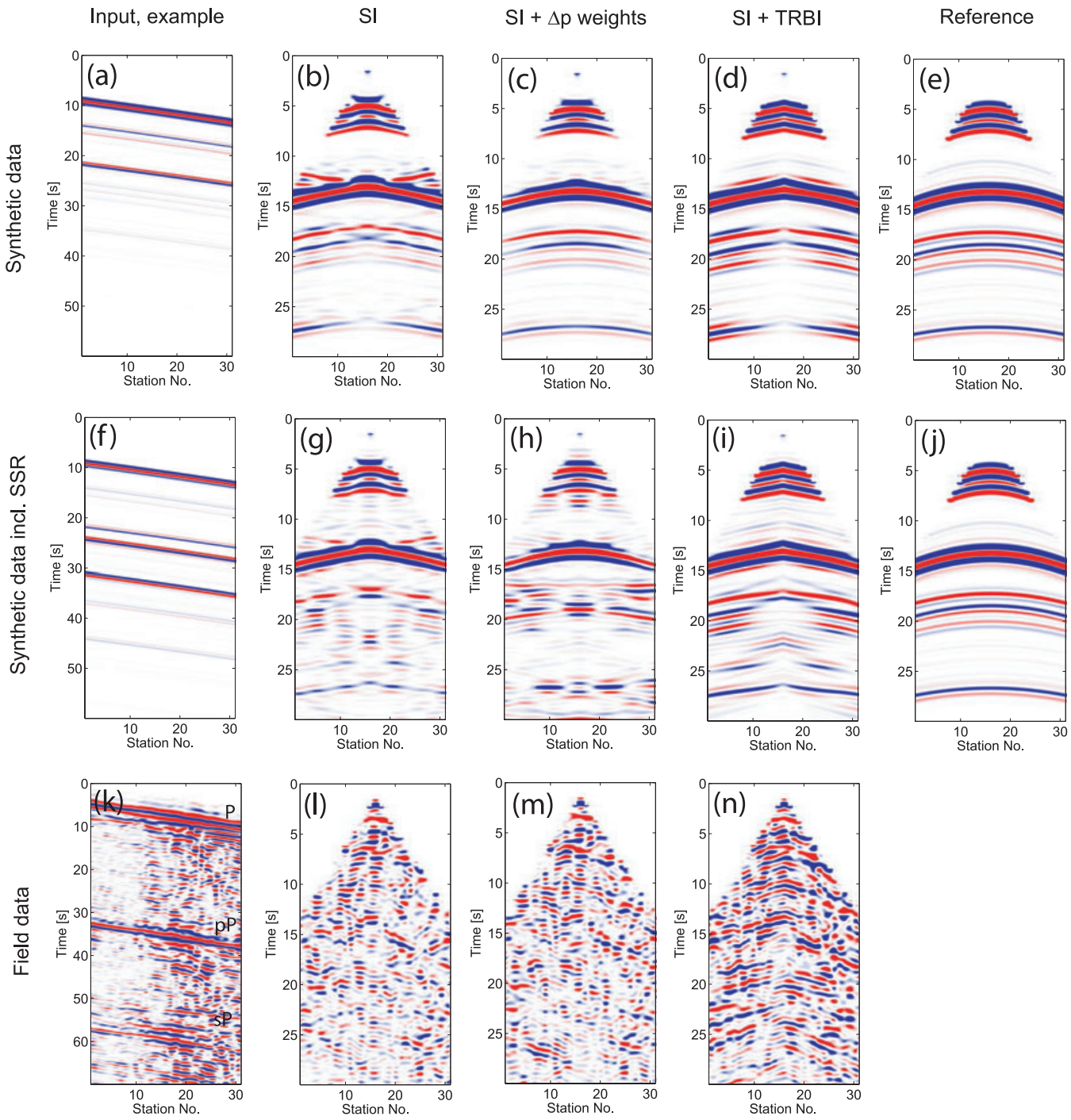

Figure 5. (a) An example of the input for seismic interferometry (SI), an isolated phase response. (b)–(d) Estimations of the reflection response, with the three different SI approaches (see the main text for explanation). (e) The partially-muted directly modeled response for a source at receiver position 16. (g)–(i) Again a comparison of the three different SI approaches, but now source-side reverberations are included in the input, of which (f) is an example. (j) A repetition of the reference response (e). (l)–(n) A comparison of the same three SI approaches, but now with the composite phase responses from the Laramie field data set as an input, of which (k) is one example.

to deal with the irregular source sampling. The retrieved responses are compared with a reference response (Fig. 5e) which is obtained by directly modelling the reflection response of a source at receiver position 16. In Fig. 5(e), primary reflections from all four interfaces can be distinguished, as well as first-order multiples from the upper three interfaces. Data at early times, bounded by $\pm h_{\max}(t)$ (see eq. 8) has been muted.

Figs 5(b) and (c) show responses retrieved with eq. (4) after adding the time-reversed acausal result to the causal part and muting data at early times. In Fig. 5(b), nothing is done to take the source irregularity into account and, as a result, large artefacts can be seen. Overillumination leads here to artefacts at times before an actual reflection and with a slope opposite to the actual reflection. Underillumination (at small ray parameters) leads here to small spurious

additions to the retrieval in the near-offset. Note the onset of the Moho reflection (the blue line at $t \approx 13$ s) being more pronounced between station number 13 and 19. This is because of incomplete addition and cancellation in the stationary-phase region. When writing integral eq. (4) as a sum, the infinitesimally small line element, dp, is replaced by a finite one, Δp. Hence, we would need to weigh the contribution of each effective source p_i by $\Delta p_i = |p_{i+1} - p_{i-1}|/2$, where p_{i+1} and p_{i-1} are the two neighbouring effective sources. By implementing Δp weights (Fig. 5c), illumination artefacts are suppressed. When the TRBI approach is used (Fig. 5d), without Δp weights, also the irregularity artefacts are suppressed, but, additionally, amplitudes in the near-offset range are weakened. This is because the stationary-phase regions for events in the near-offset range are only partly sampled. The results can better be understood by studying visualizations of the integrands, see Appendix D.

With the above application of SI, a lithospheric reflection response is obtained from receiver-side reverberations (RSR). However, the lithosphere near the source will be just as heterogeneous and lead to SSR. For example, a direct P phase is followed, for intermediate to deep earthquakes, by two SSR from the free surface: the pP and sP phases. Only for very deep earthquakes, pP and sP arrive late enough such that their RSR can be untangled from the P-phase response. Only for very shallow earthquakes, the SSR can be treated as part of the STF. Hence, for most earthquakes, we would need to replace $G(\mathbf{x}_\mathcal{A}, p, -t)$ in eq. (4) by a sum of effective phase responses, $G_P(\mathbf{x}_\mathcal{A}, p, -t) + G_{pP}(\mathbf{x}_\mathcal{A}, p, -t) + G_{sP}(\mathbf{x}_\mathcal{A}, p, -t)$, where the subscript denotes the phase, and $G(\mathbf{x}_\mathcal{B}, p, t)$ by similar terms. The resulting integral can be split up in a part that gives physical contributions to the retrieved result.

$$\int [G_P(\mathbf{x}_\mathcal{A}, p, -t) * G_P(\mathbf{x}_\mathcal{B}, p, t) + G_{pP}(\mathbf{x}_\mathcal{A}, p, -t) * G_{pP}(\mathbf{x}_\mathcal{B}, p, t) + G_{sP}(\mathbf{x}_\mathcal{A}, p, -t) * G_{sP}(\mathbf{x}_\mathcal{B}, p, t)]\mathrm{d}p, \quad (9)$$

and a part that contains only spurious cross terms

$$\int [G_P(\mathbf{x}_\mathcal{A}, p, -t) * G_{pP}(\mathbf{x}_\mathcal{B}, p, t) + G_P(\mathbf{x}_\mathcal{A}, p, -t) * G_{sP}(\mathbf{x}_\mathcal{B}, p, t) + G_{pP}(\mathbf{x}_\mathcal{A}, p, -t) * G_P(\mathbf{x}_\mathcal{B}, p, t) + G_{pP}(\mathbf{x}_\mathcal{A}, p, -t) * G_{sP}(\mathbf{x}_\mathcal{B}, p, t) + G_{sP}(\mathbf{x}_\mathcal{A}, p, -t) * G_P(\mathbf{x}_\mathcal{B}, p, t) + G_{sP}(\mathbf{x}_\mathcal{A}, p, -t) * G_{pP}(\mathbf{x}_\mathcal{B}, p, t)]\mathrm{d}p. \quad (10)$$

The application of SI needs to be such, that spurious cross terms are adequately suppressed. To show the limitations imposed by these cross terms we create a new synthetic data set which does not only contain an irregular distribution of effective sources, but which also contains SSR. The SSR are modelled for earthquake depths varying randomly between 10 and 150 km. One of the 69 composite transmission responses is shown in Fig. 5(f).

In Figs 5(g)–(i) again the same approaches are tested as in Figs 5(b)–(d), but now the composite transmission responses are used. For all approaches, a degradation of the quality of the retrieved responses can be noted, due to additional cross terms (eq. 10). Still, the actual reflection response prevails. This is because, for each earthquake, the SSR are different due to the varying depth of hypocentres and the varying source-side lithology. (In the modelling, the source-side lithology is not varied, though). The cross terms are therefore quite successfully suppressed when 69 phase responses are used (Fig. 5g), but they remain more prominent when contributions from different sources are weighted differently (Fig. 5h). The remnants of the cross terms can be noted here as cross-shaped artefacts. Note, for example, the feature overlaying an actual arrival between 25 and 29 s. The TRBI approach (Fig. 5i) gives the best results. Since no weights are applied and cross terms at negative times are rejected, the spurious events are strongly suppressed. Only at near-offsets, where the actual events are retrieved with a weakened amplitude, spurious events can be noted. The results can be understood better by studying visualizations of the integrands, see Appendix D.

Fig. 5(k) depicts the first 70 s of one actual transmission response from the Laramie data set. This response is a mixture of the P, pP and sP phases and their RSR. For this earthquake, the STF is surprisingly transient. At receiver numbers larger than 11 strong near-surface reverberations are recorded, due to the presence of a sedimentary basin.

In Figs 5(l)–(n) again the same approaches are tested as in Figs 5(g)–(i), but now the actual transmission responses are used. After applying SI, the retrieved responses are deconvolved with an effective STF estimated from the response retrieved at station 16 (the virtual source). At the sedimentary basin, near-surface reverberations are suppressed by using a larger deconvolution window. Although the actual subsurface below the Laramie array is far more complicated than the model used for the synthetics (Fig. 4b), the retrieved results (Figs 5l–n) are consistent with the modelling results with composite transmission responses (Figs 5g–i). In Fig. 5(l), spurious events can be noted. That is, normally one may expect reflections to have an increasing time with offset, but in Fig. 5(l) events can be seen that have an opposite move-out. When Δp weights are used (Fig. 5m), the spurious events are amplified. When TRBI is applied (Fig. 5n), most events with an erroneous move-out disappear and clear reflection-like events become visible. Similarly as with the modelling results, the near-offset data exhibit a weaker amplitude. From the move-out of the reflections as in Fig. 5(n), a velocity model can be derived, which is later used to migrate the reflections to the correct depth. From Figs 5(l) and (m) or from RF data it would be much harder or even impossible, to derive a velocity model.

In Fig. 5, blue and red denote positive and negative amplitudes, respectively. For the modelling we used a first derivative of a Gaussian wavelet as an STF [$s(t)$]. This can be seen in Figs 5(a) and (f) where each arrival is convolved with a blue-red alteration (plus a small sidelobe). The STF of a reconstructed primary reflection (Figs 5b–d and g–i) can be written as

$$s(-t) \times \{\pm s(t)\}, \quad (11)$$

which is a Ricker wavelet (i.e. minus the second derivative of a Gaussian wavelet) if both STFs in eq. (11) have the same sign. The reflection is constructed by a crosscorrelation of an arrival with another arrival that has bounced once more at the free surface. When the reflection is from an interface with an increase in impedance with depth, the second STF in eq. (11) will have the opposite sign from the first one, because of the extra free-surface bounce. Hence, the effective STF will be blue-red-blue [see, e.g. the Moho reflection at $t = 14$ s in Fig. 5(b)]. When the reflection is from an interface with a decrease in impedance with depth, the second STF in eq. (11) will have the same sign as the first one, since it encounters a negative reflection coefficient two times more. Hence, the effective STF will be red-blue-red [see, e.g. the second reflection in Fig. 5(b), at $t = 7$ s]. Also the effective wavelet for the field data resembles a Ricker wavelet, after applying SI and STF deconvolution. In theory, the deconvolution would lead to a Gaussian wavelet. In practice,

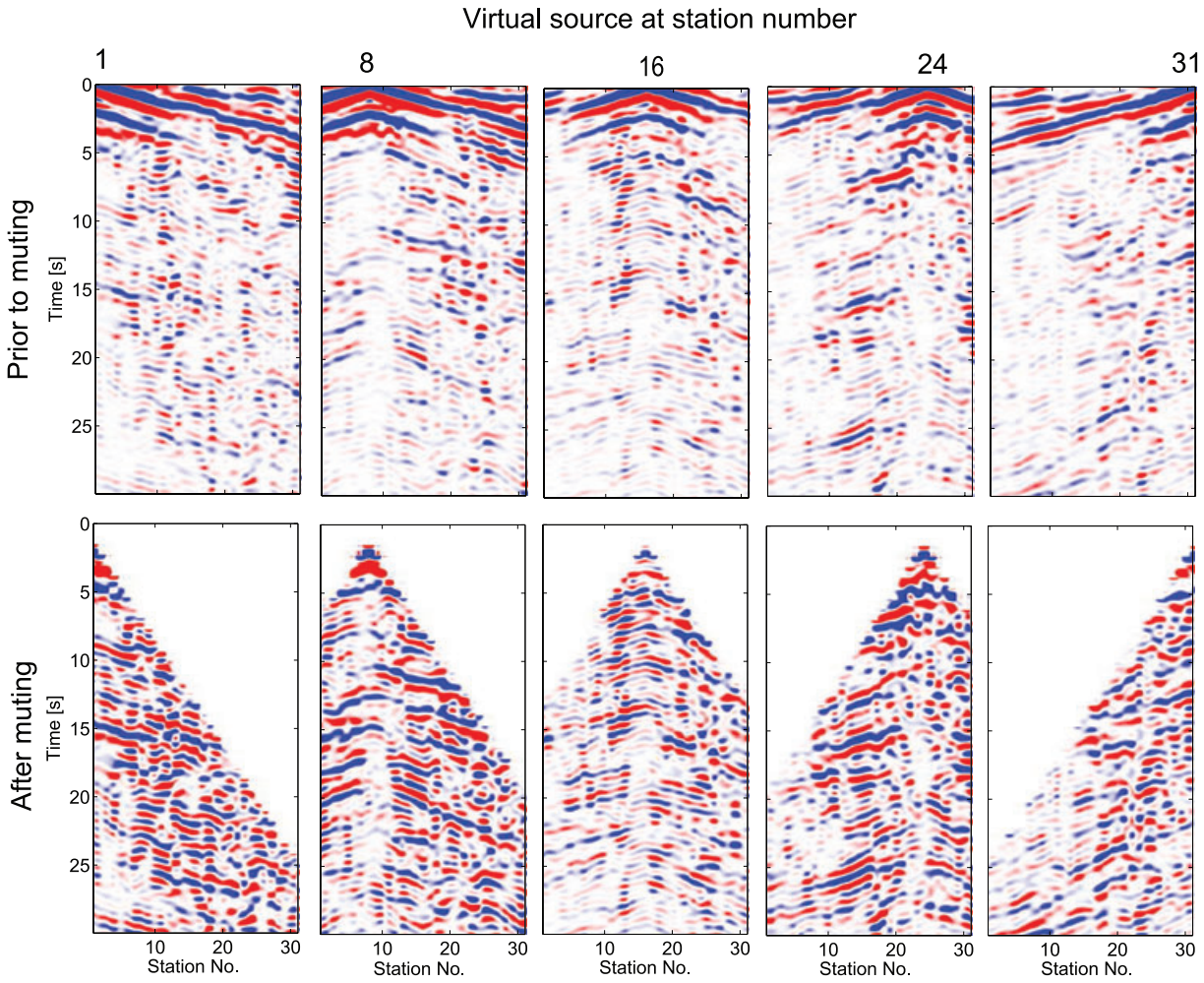

Figure 6. Retrieved responses for a virtual source at, from left to right, receiver number 1, 8, 16, 24 and 31. On the top and bottom, respectively, the raw and muted retrieved responses are shown.

extra ringing is introduced and the wavelet looks more like a Ricker wavelet. As for the synthetic data, a positive Ricker wavelet denotes an impedance decrease with depth.

In Fig. 6, five responses are shown, which are retrieved from the Laramie transmission data with the application of TRBI. On the top panels, the near-surface phases are especially pronounced. The first clear arrival in the panels, which looks like a direct wave, is in fact correlation noise (eq. 7), which result from remnants of crosscorrelations of direct waves at the edges of the illumination distribution (Ruigrok *et al.* 2008). Apart from illumination considerations, the phase can also be judged to be spurious by its, for a direct wave, unphysical apparent velocity of $v_{p1} \approx 20$ km s^{-1}. On all top panels, a hyperbolic event can be seen at $t \approx 2.5$ s. This is a reflection from a large contrast in the upper crust, at $x_3 \approx 5$ km. Only in the near-offset, the move-out of this reflection is retrieved correctly. On the lower panels, the retrieved responses are shown after muting data at early times, bounded by $\pm h_{\max}(t)$ (see eq. 8). Hence, strong unphysical events are removed. In the response after muting, we may expect to see reflections and multiples, retrieved with the actual kinematics, as for the synthetic data (Fig. 5i). Nevertheless, also here an imprint of correlation noise still remains, partly caused by ringing from near-surface interfaces. In the next section, panels as in Fig. 6 will be used for further processing.

5 IMAGING

In this section, we further process the retrieved reflection responses into images, using standard exploration-geophysics processing (Yilmaz & Doherty 2000). We repeat SI with TRBI (Fig. 5n) to retrieve responses for a source at each of the 31 receiver locations. We resort the retrieved shot gathers to common-midpoint (CMP) gathers. Next, we estimate a 2-D *P*-wave velocity model for the deeper subsurface. Velocities are estimated from the move-out of primary reflections in the CMP gathers, through a semblance velocity analysis.

We start with processing the synthetic data. Fig. 7(a) depicts a CMP gather (left-hand panel) for the midpoint position coinciding with station 12 (see Fig. 3a), its semblance (middle panel) and the stack over half-offset after normal-move-out (NMO) correction (right-hand panel). If we denote a CMP panel in the time domain as $f^{\rm CMP}(t, h)$, where h is the half-offset, we can write the NMO-corrected function for different velocities v_p as $f^{\rm NMO}(t, h, v_p)$. We define the semblance f^S [as a variation of the one defined in Neidell & Taner (1971)] as the following weighted stack of $f^{\rm NMO}(t, h, v_p)$ over half-offset:

$$f^S(t, v_p) = \frac{\left(\sum_h f^{\rm NMO}(t, h, v_p)\right)^2}{\sum_h \left(f^{\rm NMO}(t, h, v_p)\right)^{1.5}}, \tag{12}$$

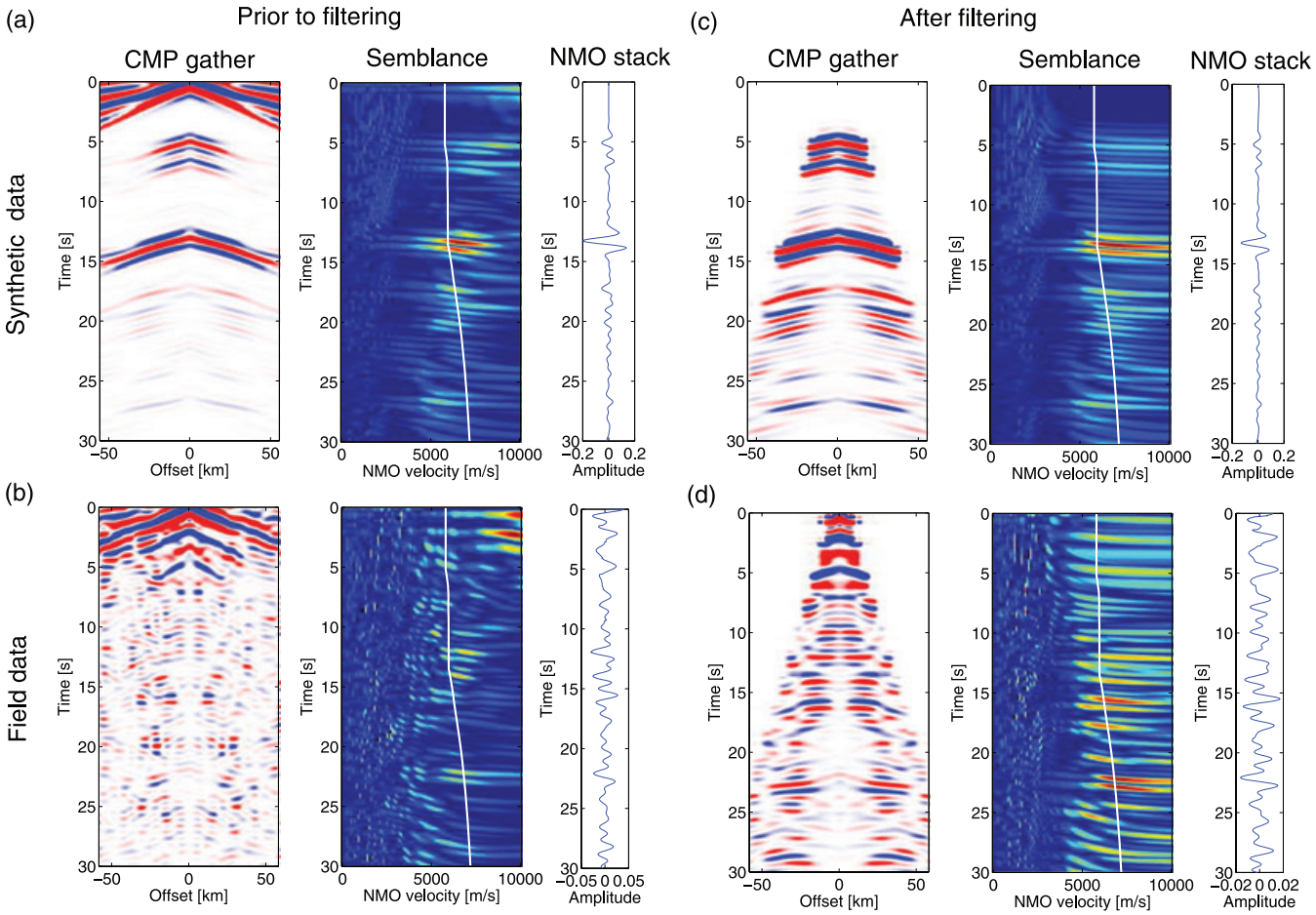

Figure 7. A common-midpoint gather, retrieved with seismic interferometry, for the midpoint position coinciding with station 12 (left-hand panel), its semblance (middle panel) and normal-move-out stack (right-hand panel), using the model velocity function $v_p(t)$ as depicted by the white line in the semblance plot (middle panel). The same three panels are shown for the synthetic data (a), the field data (b) and the synthetic and field data after filtering, (c) and (d), respectively.

which weighted stack is implemented with sliding time windows with a duration of the dominant period in the signal. In eq. (12), there is a power of 1.5 in the denominator instead of a more common power of 2. By using a reduced power, events with a higher amplitude in $f^{\mathrm{CMP}}(t, h)$ are also emphasized in the semblance. Because of a limited sampling in half-offset, the semblance is aliased for small velocities.

In the semblance plot, a velocity function (white line) is drawn that corresponds to the actual velocities of the model that were used for computing the synthetics (Fig. 4b). During the first 10 s the velocity is overestimated by picking the highest amplitudes in the semblance. This is because near-surface reflections are retrieved with an erroneous move-out at larger offsets. At times later than 10 s the velocities can be estimated reasonably well from the semblance, until the time (≈20 s) when multiples start arriving.

The NMO stack can be written as $\sum_h f^{\mathrm{NMO}}[t, h, v_p(t)]$. For the velocity function $v_p(t)$ the actual velocities are used (the white line in the semblance figure). If the correct velocities are used, the move-out of the reflections in $f^{\mathrm{CMP}}(t, h)$ are perfectly removed and the NMO stack is an estimate of the response as if there were a coinciding receiver and source at the free surface (in this case at station location 12). In the stacking process noise and multiples are suppressed to a large extend.

Fig. 7(b) depicts the same type of panels as in Fig. 7(a) but now for the field data. For these data, the CMP gather (left-hand panel) looks a lot more complicated and noisier. Besides primary reflections, the CMP gather also contains multiples and correlation noise (eq. 7), which are both noise for an imaging scheme for primary reflections. In the semblance panel (middle panel) it is now hard to pick velocities. Therefore the data are filtered prior to velocity analysis. A filtering approach as described by Ryu (1982) is taken to suppress the noise. Each CMP gather is NMO corrected with a velocity function that is between the velocities of the primaries and multiples. Subsequently, after a temporal and spatial Fourier transform, the data at positive wavenumbers are removed and the remaining data are inverse Fourier transformed and inverse NMO corrected. Consequently, events with low apparent velocities are removed. This approach is successful in removing parts of the correlation noise, but the move-out discrimination between primaries and multiples is often not large enough to remove the multiples. To remove more correlation noise, another wavenumber filter is applied. It is assumed that at positive offsets, the move-out of arrivals is also positive. Therefore the data at negative wavenumbers are removed for the positive offsets, and similarly the data at positive wavenumbers are removed for the negative offsets. In the last filtering step, just like for Fig. 6 (bottom panel), data at early times is removed.

Fig. 7(c) depicts the same type of panels as in Fig. 7(a) but now after filtering. Comparing Fig. 7(c) with 7(a) reveals that artefacts with erroneous move-out have been suppressed. In the semblance

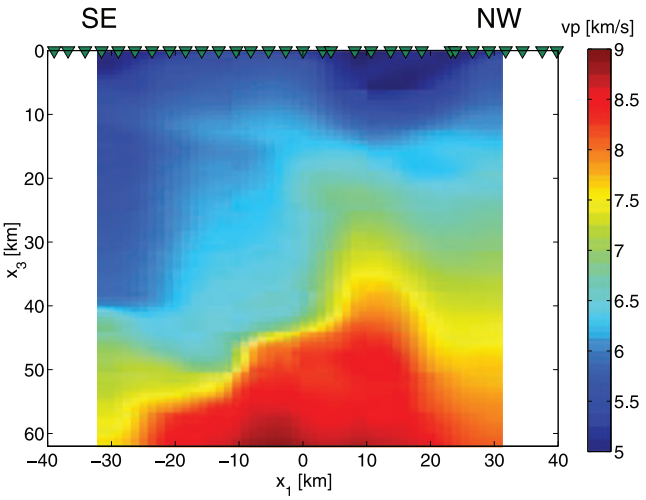

Figure 8. Estimated velocity model of the lithosphere below the Laramie array.

panel, some resolution in v_p has been lost through the filtering, but the maxima better follow the actual velocity trend (the white line). For the NMO stack in Fig. 7(c) it can be seen that the wavelet has improved. The Moho reflection in Fig. 7(c) ($t = 14$ s) better resembles a minus Ricker wavelet than in Fig. 7(a).

Fig. 7(d) depicts the same type of panels as in Fig. 7(b) but now after filtering. Comparing Fig. 7(d) with 7(b) reveals that artefacts with erroneous move-out have been suppressed. In Fig. 7(d) reflections are now visible that were largely hidden by correlation noise in Fig. 7(b). The semblance in Fig. 7(d) is now much better suited for picking a velocity trend than in Fig. 7(b). Despite the large differences between the CMP gathers and the semblances in Figs 7(b) and (d), the NMO stacks are still quite similar, since in Fig. 7(d) especially noise has been removed that does not show up in the stack.

We repeat the semblance velocity analysis as in Fig. 7 for all CMP gathers with sufficient fold. Next, we compute the interval velocities from the estimated rms velocities (Dix 1955). The resulting 1-D velocity profiles are concatenated and smoothed with a median filter. Since reflections from shallow reflectors could only be retrieved at a limited offset, the CMP gathers cannot be used to reliably estimate the velocities in the upper crust [$x_3 = (0, 10)$ km]. Fig. C1 depicts the near-surface velocity functions, as were estimated in the decomposition process (Appendix C). The velocities are an average of the local velocities right under the receivers and are used as an estimate for the velocities in the upper 10 km. The combined velocity model, derived from the decomposition ($x_3 <=10$ km) and the semblance analysis ($x_3 > 10$ km) is depicted in Fig. 8.

The CMP gathers close to the first and the last receiver are discarded due to limited fold. All other CMP gathers are NMO corrected and stacked to obtain pseudo-zero-offset data. These are the responses as if there were coinciding receivers and sources at the free surface. In Fig. 9 the pseudo-zero-offset data are depicted for the synthetic data (a) and the field data (b). The pseudo-zero-offset data are consecutively poststack Kirchhoff time migrated (Bleistein 1999) and time-to-depth converted to obtain reflectivity images as a function of depth (Figs 9c and d). For the latter two steps, the data-derived velocity model (Fig. 8) is used for the field data. For the synthetic data, the velocity model as depicted in Fig. 4(b) is used.

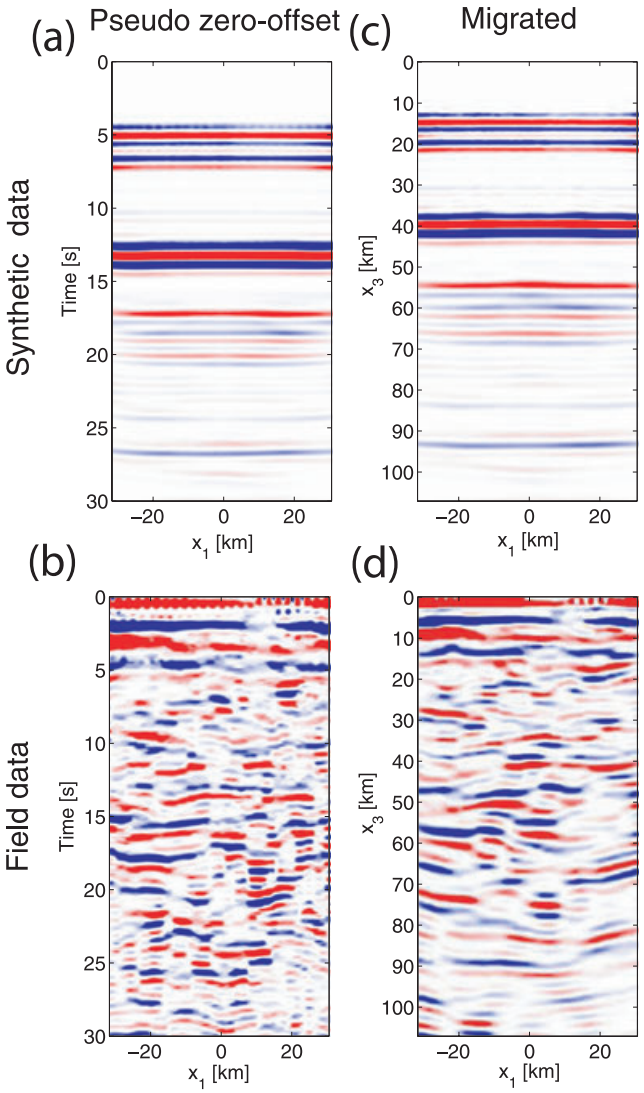

Figure 9. Pseudo-zero-offset data for (a) the synthetic data and (b) the field data. Post-stack migrated and time-to-depth converted images for (c) the synthetic data and (d) the field data. The horizontal axis is labeled with the inline position with respect to the middle receiver, which position is negative for receivers at the SE side and positive for receivers at the NW side. In (a) and (b) the vertical coordinate denotes two-way traveltime.

Comparing the final image obtained from the synthetic data in Fig. 9(c) with the model in Fig. 4(b), it can be seen that all interfaces are imaged at the correct depth, despite the limited and irregular illumination and despite the SSR. Additionally, below 55 km depth, multiples have caused spurious interfaces. The image obtained from the field data (Fig. 9d) might similarly be affected by multiples at larger depths. Moreover, the migration leads to finite aperture artefacts at depths larger than the length of the array. To limit both possible reasons for misinterpretation, the image is restricted to 64 km depth. Fig. 10 displays this restricted image with the same scaling on both axes and a cropping of the stronger amplitudes (in the near surface). In Appendix E it is shown that the shallow reflectors in this image are consistently found for varying amounts of phase responses. The deeper reflectors, though, only become visible when a large number of phase responses is used. Only for a large amount of phase responses, the spurious events caused by SSR are sufficiently suppressed.

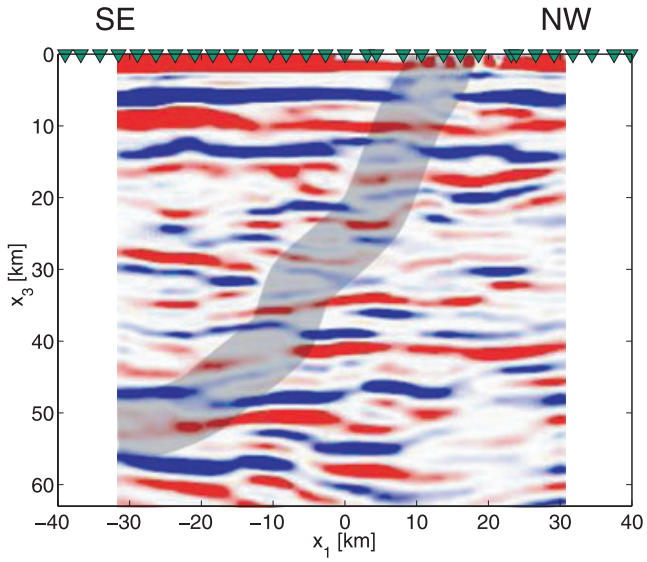

Figure 10. The reflectivity image of the subsurface below the Laramie array, obtained by seismic interferometry. A blue-red-blue alternation may be interpreted as an interface with an increase in velocity with depth. An interpretation of the Cheyenne Belt is denoted by the dipping grey zone.

Fig. 10 shows a layered upper crust on top of a highly fragmented lower crust. A striking feature in the upper crust is a reduced reflectivity, near $x_1 \approx 10$ km. This zone of lower reflectivity likely continues through abrupt discontinuities in the lower crust and upper mantle, as highlighted by the grey shading. The position where this zone hits the surface is very close to where the Cheyenne Belt is expected from observations in the field (Hansen & Dueker 2009). Thus, the grey shading in Fig. 10 is interpreted as the suture zone between Archean and Proterozoic terranes, on the NW and SE side, respectively. Consistent with an interpretation from Karlstrom & Humphreys (1998), the Proterozoic terrane is the upper plate. Because reflections from this zone have $|p| > 0.08$ s km^{-1}, this fault zone is not directly imaged with our limited illumination (Fig. 4a). As the Moho depth in the area is expected at ≈40 km depth (Chulick & Mooney 2002), we interpret the undulating feature at 42 km depth as the Moho. This Moho starts abruptly NW of the suture zone and is therefore interpreted to be Archean. Below 42 km still a chaotic distribution of apparent interfaces can be seen. A part of these might be caused by free-surface multiples from strong reflectors in the upper crust. A part of the features below 42 km might also be explained by underthrusting Proterozoic lower crust, as in Hansen & Dueker (2009).

Comparing Fig. 10 with the RF images from Hansen & Dueker (2009), similar large features are noticeable, but clearly SI leads to a higher-resolution image. Especially within the crust, much more detail can be seen in the SI image. For example, the interface at 28 km depth between $x_1 \approx [-32, -12]$ km cannot be seen in the RF images. Moreover, with SI, the interfaces might have been migrated to a more accurate position, since a data-derived velocity model was used.

The final SI image may still be improved by pre-stack depth migration rather than poststack time migration and by using a more advanced multiple-elimination scheme (Verschuur 2006), although multiple removal on land is a notoriously difficult problem that requires dense sampling.

6 CONCLUSIONS

We studied the retrieval of reflections between the receivers of a regional array of broad-band stations using SI. SI consists of correlations of observations at different receiver locations, followed by an integration of the correlation results. It is necessary to record enough effective sources from actual earthquakes to adequately sample this integral. For this reason, we used *P* phases complemented by *PP*, *PcP* and *PKP*, where the latter three phases are used to fill up the gaps in the illumination of the *P* phases. We showed first that a few months of data suffice to select an adequate distribution of phase responses, at least when the array is approximately in-plane with an earthquake belt. The irregularity of the phase distribution introduces over- and under-illumination artefacts to the retrieved responses. We showed that these artefacts can be suppressed by weighing the contributions to the integrand with the distances between the effective sources. When, in addition, the influence of source-side reverberations is taken into account, the weighing strategy turns out to degrade the retrieved response. We showed that, for this case, a better reflection response can be obtained when contributions from effective sources with either positive or negative ray parameters are time-reversed prior to integration. Using velocity analysis and seismic migration we further turned the retrieved body-wave responses into a reflectivity image. A high-resolution image was obtained from the lithosphere below the Laramie array with similar features as interpreted by other researchers from receiver-function images. Especially at larger depths, ghost interfaces caused by multiples were still present in the image. On the reflectivity image, we could track the Cheyenne Belt, a suture zone between Archean and Proterozoic terranes.

ACKNOWLEDGMENTS

The research of ER was financially supported by The Netherlands Organization for Scientific Research NWO (grant Toptalent 2006 AB) and by the Netherlands Research Centre for Integrated Solid Earth Science (ISES); the research of D.D. by the Dutch Technology Foundation STW (grant VENI.08115). We would like to thank IRIS and the people involved with the Laramie array for providing the data. Also we are grateful to the developers of JWEED, mmap, ttbox and CREWES Matlab for delivering great software to the geoscience community. Finally, we would like to thank the reviewers for their stimulating comments.

REFERENCES

Abe, S., Kurashimo, E., Sato, H., Hirata, N., Iwasaki, T. & Kawanaka, T., 2007. Interferometric seismic imaging of crustal structure using scattered teleseismic waves, *Geophys. Res. Lett.,* **34,** L19305, doi:10.1029/2007GL030633.

Bleistein, N., 1999. Hagedoorn told us how to do Kirchhoff migration and inversion, *Leading Edge,* **18,** 918–927.

Bostock, M., 2004. Green's functions, source signatures, and the normalization of teleseismic wave fields, *J. geophys. Res.,* **109,** B03303, doi:10.1029/2003JB002783.

Bostock, M. & Rondenay, S., 1999. Migration of scattered teleseismic body waves, *Geophys. J. Int.,* **137,** 732–746.

Campillo, M. & Paul, A., 2003. Long-range correlations in the diffuse seismic coda, *Science,* **299,** 547–549.

Chulick, G. & Mooney, W., 2002. Seismic structure of the crust and uppermost mantle of North America and adjacent oceanic basins: a synthesis, *Bull. seism. Soc. Am.,* **92,** 2478–2492.

Claerbout, J., 1968. Synthesis of a layered medium from its acoustic transmission response, *Geophysics,* **33,** 264–269.

Derode, A., Larose, E., Campillo, M. & Fink, M., 2003a. How to estimate the Green's function of a heterogeneous medium between two passive sensors? Application to acoustic waves, *Appl. Phys. Lett.,* **83,** 3054–3056.

Derode, A., Larose, E., Tanter, M., de Rosny, J., Tourin, A., Campillo, M. & Fink, M., 2003b. Recovering the Green's function from field-field correlations in an open scattering medium, *J. acoust. Soc. Am.,* **113,** 2973–2976.

Dix, C., 1955. Seismic velocities from surface measurements, *Geophysics,* **20,** 68–86.

Draganov, D., Wapenaar, K. & Thorbecke, J., 2006. Seismic interferometry: reconstructing the Earth's reflection response, *Geophysics,* **71,** SI61–SI70.

Draganov, D., Campman, X., Thorbecke, J., Verdel, A. & Wapenaar, K., 2009. Reflection images from seismic noise, *Geophysics,* **74,** A63–A67.

Draganov, D., Ghose, R., Ruigrok, E., Thorbecke, J. & Wapenaar, K., 2010. Seismic interferometry, intrinsic losses and Q-estimation, *Geophys. Prospect.,* **58,** 361–373.

Dueker, K. & Zurek, B., 2001. Thick-structured proterozoic lithosphere of the Rocky Mountain region, *GSA Today,* **11,** 4–9.

Fan, C., Pavlis, G., Weglein, A. & Nita, B., 2006. Removing free-surface multiples from teleseismic transmission and constructed reflection responses using reciprocity and the inverse scattering series, *Geophysics,* **71,** SI71–SI78.

Hansen, S. & Dueker, K., 2009. P- and S-wave receiver function images of crustal imbrication beneath the Cheyenne Belt in southeast Wyoming, *Bull. seism. Soc. Am.,* **99,** 1953–1961.

Karlstrom, K. & Humphreys, E., 1998. Persistent influence of Proterozoic accretionary boundaries in the tectonic evolution of southwestern North America: interaction of cratonic grain and mantle modification events, *Rocky Mt. Geol.,* **33,** 161–179.

Kennett, B., 1991. The removal of free surface interactions from three-component seismograms, *Geophys. J. Int.,* **104,** 153–163.

Knapmeyer, M., 2004. TTBox: a Matlab toolbox for the computation of 1D teleseismic travel times, *Seism. Res. Lett.,* **75,** 726–733.

Kumar, M. & Bostock, M., 2006. Transmission to reflection transformation of teleseismic wavefields, *J. geophys. Res.,* **111,** B08306, doi:10.1029/2005JB004104.

Langston, C., 1977. Corvallis, oregon, crustal and upper mantle receiver structure from teleseismic P and S waves, *Bull. seism. Soc. Am.,* **67,** 713–724.

Neidell, N. & Taner, M., 1971. Semblance and other coherency measures for multichannel data, *Geophysics,* **36,** 482–497.

Nowack, R., Dasgupta, S., Schuster, G. & Sheng, J.-M., 2006. Correlation migration using Gaussian beams of scattered teleseismic body waves, *Bull. seism. Soc. Am.,* **96,** 1–10.

Ruigrok, E., Draganov, D., Thorbecke, J., van der Neut, J. & Wapenaar, K., 2008. Sampling and illumination aspects of seismic interferometry in horizontally layered media, Extended abstracts, P277, EAGE.

Ruigrok, E., Wapenaar, K., van der Neut, J. & Draganov, D., 2009. A review of crosscorrelation and multidimensional deconvolution seismic interferometry for passive data, Extended abstracts, A09, EAGE.

Ryu, J., 1982. Decomposition (decom) approach applied to wave field analysis with seismic reflection records, *Geophysics,* **47,** 869–883.

Schuster, G., 2009. *Seismic Interferometry*, Cambridge University Press, Cambridge, United Kingdom.

Schuster, G., Yu, J., Sheng, J. & Rickett, J., 2004. Interferometric/daylight seismic imaging, *Geophys. J. Int.,* **157,** 838–852.

Snieder, R., 2004. Extracting the Green's function from the correlation of coda waves: a derivation based on stationary phase, *Physical Review E,* **69,** 046610-1–046610-8.

Spetzler, J. & Snieder, R., 2004. Tutorial: the Fresnel volume and transmitted waves, *Geophysics,* **69,** 653–663.

Tonegawa, T., Nishida, K., Watanabe, T. & Shiomi, K., 2009. Seismic interferometry of teleseismic S-wave coda for retrieval of body waves: an application to the Philippine Sea slab underneath the Japanese Islands, *Geophys. J. Int.,* **178,** 1574–1586.

Verschuur, D., 2006. *Seismic Multiple Removal Techniques: Past*, *Present and Future*, EAGE, Houten, the Netherlands.

Wapenaar, K., 2004. Retrieving the elastodynamic Green's function of an arbitrary inhomogeneous medium by cross-correlation, *Phys. Rev. Lett.,* **93,** 254301-1–254301-4.

Wapenaar, K. & Fokkema, J., 2006. Green's functions representations for seismic interferometry, *Geophysics,* **71,** SI33–SI46.

Wapenaar, K., Draganov, D. & Robertsson, J., 2008. *Seismic Interferometry: History and Present Status*, SEG, Tulsa, OK, USA.

Wilson, D. & Aster, R., 2005. Seismic imaging of the crust and upper mantle using regularized joint receiver functions, frequency-wave number filtering, and multimode Kirchhoff migration, *J. geophys. Res.,* **110,** B05305, doi:10.1029/2004JB003430.

Yilmaz, O. & Doherty, S., 2000. *Seismic Data Analysis: Processing, Inversion and Interpretation of Seismic Data*, SEG, Tulsa, OK, USA.

APPENDIX A: SAMPLING

In this appendix we derive a sampling criterion for the 2-D integral representations (1), (2) and (3). First, we argue that a sufficient source sampling is important. Then, we compute the Jacobians for the change in integration variables. Thereafter, we derive a sampling criterion in dp and use the Jacobians to find sampling criteria expressed in dϕ and dx. Finally, we consider the required earthquake distribution for retrieving lithospheric reflections below the Laramie array.

For this analysis, we exploit the fact that the reference velocity model for the Earth is known. For this reason, we do not need to consider the complete Earth as an unknown heterogeneous medium (Fig. 1a), but we can directly focus on our medium of interest, the lithosphere below an array of receivers. By ray tracing through the reference model, different phases induced by teleseismic and global earthquakes can be represented as individual sources on a large semisphere surrounding the lithosphere on the receiver side [$\partial\mathbb{S}_1$ in Fig. A1 and in eqs (1) and (2)]. It would be ideal for the application of seismic interferometry (SI) if the lithosphere consisted of a distribution of point scatterers as in the experiment by Derode *et al.* (2003b) or was bounded at the lower side by a highly scattering slab, as in the experiments by Derode *et al.* (2003a). In either case, illumination with a few sources from different directions would suffice to retrieve a Green's function between two station positions placed in or upon the lithosphere. This is because the illumination of a single phase with a very narrow ray parameter band is, by

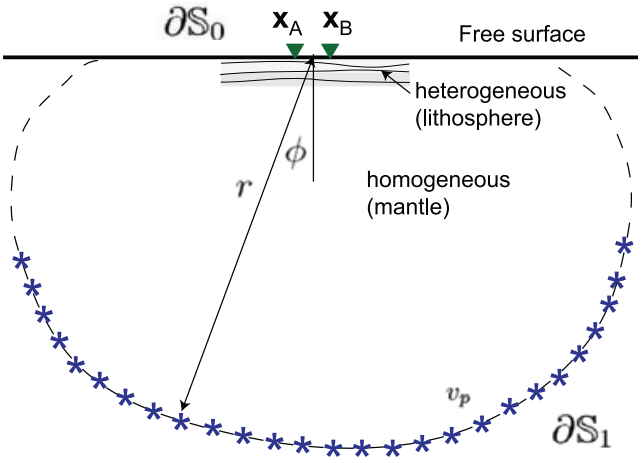

Figure A1. An effective configuration for lithospheric-scale SI. A medium with receivers (triangles) on the free surface is illuminated from below with a distribution of sources, of which the location is given in polar coordinates (r, ϕ).

multiple scattering, increased to a broad and well-sampled ray parameter band, that represents the line integral in eq. (1) or (2). Though there might be multiple scattering from point scatterers, especially in the crust, a more conventional depiction of the convergence zone and lithosphere is that of an approximately spherically layered medium. For a 1-D layered medium, there are no scatterers (Huygens sources) adding ray parameters to the transmission responses. Therefore, the source surface $\partial\mathbb{S}_1$ (Fig. A1) needs to be sufficiently covered with effective sources. $\partial\mathbb{S}_1$ may have an arbitrary shape as long as it represents a sufficient illumination aperture.

The distance between a source $\mathbf{x}_i$ and its neighbouring source $\mathbf{x}_{i+1}$ on $\partial\mathbb{S}_1$ is $dx = |\mathbf{x}_i - \mathbf{x}_{i+1}|$. The same separation can be expressed in source angle as $\mathrm{d}\phi = |\phi_i - \phi_{i+1}|$ or in ray parameter as $\mathrm{d}p = |p_i - p_{i+1}|$. For finding the relation between $\mathrm{d}x$, $\mathrm{d}\phi$ and $\mathrm{d}p$, we compute the Jacobians for a change of integration from (x_1, x_3) to (r, ϕ):

$$J_1 = \left|\frac{\partial(x_1, x_3)}{\partial(r, \phi)}\right| = r, \tag{A1}$$

and using that $p = \sin\phi / v_p$, for a change of integration from (r, ϕ) to (r, p)

$$J_2 = \left|\frac{\partial(r, \phi)}{\partial(r, p)}\right| = \partial_p \phi = \frac{v_p}{\sqrt{1 - v_p^2 p^2}}. \tag{A2}$$

Hence, for sources on the line $\partial\mathbb{S}_1$ we find

$$\mathrm{d}x = r\mathrm{d}\phi = \frac{r v_p}{\sqrt{1 - v_p^2 p^2}}\mathrm{d}p. \tag{A3}$$

The retrieval of arrivals between two receiver positions is achieved by the crosscorrelation and stacking of arrivals in the transmission responses with similar ray paths. When ray paths coincide, the derivative of the phase with respect to the source coordinate is stationary. In the stationary-phase region (the Fresnel zone around the stationary phase) we only need limited sampling. Outside this region, though, the derivative with respect to the source coordinate increases (see Appendix D). The sampling of the sources needs to be such that the non-stationary contributions interfere destructively. This destructive interference will happen when, after crosscorrelation, the time difference between a contribution from two neighbouring sources is smaller than half the minimum period.

$$\mathrm{d}t < \frac{1}{2 f_{\max}}. \tag{A4}$$

A transmission response contains many different arrivals, of which the direct wave ($^{\mathrm{dw}}$) and ghost reflections ($^{\mathrm{gh}}$) are the most relevant for body-wave SI. Two direct waves between source $\mathbf{x}_i$ and receivers $\mathbf{x}_\mathcal{A}$ and $\mathbf{x}_\mathcal{B}$ can be described with their ray parameters, $p^{\mathrm{dw}}_{\mathcal{A},i}$ and $p^{\mathrm{dw}}_{\mathcal{B},i}$ [Fig. A2 (left-hand panel)]. Similarly, two ghost reflections between source $\mathbf{x}_i$ and receivers $\mathbf{x}_\mathcal{A}$ and $\mathbf{x}_\mathcal{B}$ can be described as $p^{\mathrm{gh}}_{\mathcal{A},i}$ and $p^{\mathrm{gh}}_{\mathcal{B},i}$ [Fig. A2 (right-hand panel)]. If we choose the distance to the source r (Figs A1 and A2) much larger than the length of the array, the wavefield near the array will be planar. Hence, $p^{\mathrm{dw}}_{\mathcal{A},i} = p^{\mathrm{dw}}_{\mathcal{B},i}$. If we consider a layered subsurface and large r, also $p^{\mathrm{gh}}_{\mathcal{A},i} = p^{\mathrm{gh}}_{\mathcal{B},i}$. Moreover, if we only consider horizontal interfaces near the array, all arrivals will have the same ray parameter.

$$p_i = p^{\mathrm{dw}}_{\mathcal{A},i} = p^{\mathrm{dw}}_{\mathcal{B},i} = p^{\mathrm{gh}}_{\mathcal{A},i} = p^{\mathrm{gh}}_{\mathcal{B},i}. \tag{A5}$$

Hence, when eq. (A5) holds, the time difference of the wavefield caused by source $\mathbf{x}_i$, hitting upon receiver $\mathbf{x}_\mathcal{A}$ and $\mathbf{x}_\mathcal{B}$ can be expressed as

$$\mathrm{d}t_i = \frac{2h\sin(\phi_i)}{v_p} = 2hp_i, \tag{A6}$$

where h is the half offset ($h = |\mathbf{x}_\mathcal{A} - \mathbf{x}_\mathcal{B}|/2$), ϕ_i is the angle of the ray with the normal, at the source, and v_p is the velocity of the medium, at the source position. After crosscorrelation, the time difference for two neighbouring sources, $\mathbf{x}_i$ and $\mathbf{x}_{i+1}$, is

$$\mathrm{d}t = |\mathrm{d}t_i - \mathrm{d}t_{i+1}|. \tag{A7}$$

When we combine relations (A4), (A6) and (A7) we find the sampling criterion expressed in ray parameter.

$$\mathrm{d}p < \frac{1}{4 f_{\max} h_{\max}}, \tag{A8}$$

where $h_{\max}$ is the maximum half offset of interest.

Combining relation (A8) with (A3) and taking $p_{\min} = 0\ \mathrm{s\,km^{-1}}$, we find a sampling criterion expression in $\mathrm{d}\phi$

$$\mathrm{d}\phi < \frac{v_p}{4 f_{\max} h_{\max}} \tag{A9}$$

and a sampling criterion expressed in $\mathrm{d}x$

$$\mathrm{d}x < \frac{r_{\min} v_p}{4 f_{\max} h_{\max}}. \tag{A10}$$

In both expressions (A9) and (A10), the sampling is now also a function of the velocity of the medium in which the sources are, and the ray parameter. The higher the v_p, the larger the sampling in $\mathrm{d}\phi$

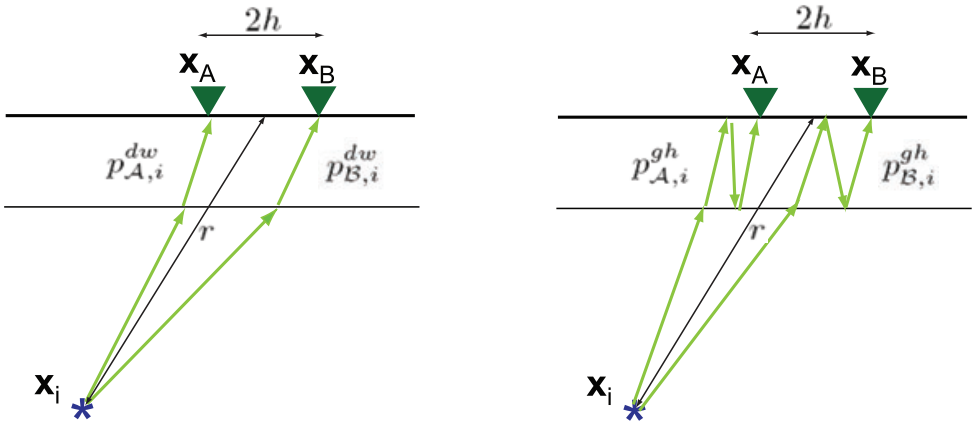

Figure A2. The ray paths for two direct waves (left-hand side) and two ghost reflections (right-hand side).

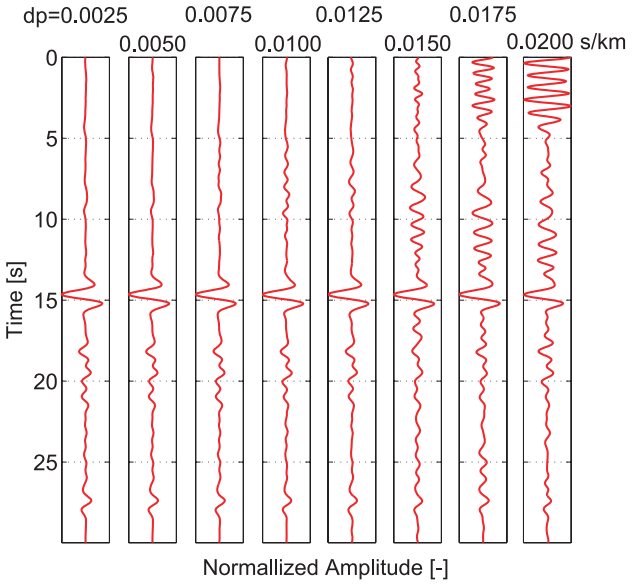

Figure A3. The result after applying SI to synthetic transmission responses, for obtaining a virtual source and a receiver at a distance of 40 km. From left to right, the ray parameter spacing of the transmission responses is increased from $\mathrm{d}p = 0.0025$ to $\mathrm{d}p = 0.0200\ \mathrm{s\,km^{-1}}$.

and $\mathrm{d}x$ may be. Furthermore, expression (A10) is also a function of the minimum radius, which radius would be constant if $\partial\mathbb{S}_1$ was a semicircle. The larger the minimum radius, the larger the sampling in $\mathrm{d}x$ may be.

For an application of SI for lithospheric-scale imaging, using teleseismic and global phases, the approximations for deriving condition (A8) are largely satisfied. When we take $h_{\max} = 20$ km (the half offset between a virtual source at the middle receiver of the Laramie array and a receiver a the edge of the array) and take $f_{\max} = 1.5$ Hz, we find $\mathrm{d}p = 0.0083\ \mathrm{s\,km^{-1}}$.

We test the derived sampling condition on synthetic data. As in Section 4, we use the simplified lithospheric model (Fig. 4b) to synthesize transmission responses with varying $\mathrm{d}p$. Fig. A3 shows the results after applying SI for obtaining a virtual source at the middle receiver and a receiver at the edge of the array ($h_{\max} = 20$ km). For $\mathrm{d}p = 0.0025$, $\mathrm{d}p = 0.0050$ and $\mathrm{d}p = 0.0075\ \mathrm{s\,km^{-1}}$ the retrieved results are almost identical. From $\mathrm{d}p = 0.0100\ \mathrm{s\,km^{-1}}$ onwards undersampling artefact start to occur, which become more pronounced for larger spacings in $\mathrm{d}p$.

By ray tracing through the PREM model (Knapmeyer 2004) we map the source sampling of $\mathrm{d}p = 0.0083\ \mathrm{s\,km^{-1}}$ to actual earthquake positions (Fig. A4). Only illumination from one side is shown, since this would be sufficient for imaging an approximately layered lithosphere. In reality, illumination from both sides would be combined to reach a better sampling and to increase the signal-to-noise ratio. If high quality data could be recorded and the STF were very transient, data from less than 11 earthquakes would be sufficient to retrieve a multidimensional reflection response. The required sampling and a sufficient illumination can be reached with *P* and *PKP* [Fig. A4(up)] or with *PP* and *PcP* [Fig. A4(down)], or with a combination of all these phases. For *P* and *PcP* phases, the maximum source spacing maps to a maximum allowed earthquake spacing of about 1000 km or $\Delta = 10^\circ$. For *PP* phases, the maximum earthquake spacing is about 20°. For *PKP* phases, the required source spacing for the actual earthquakes can be seen to be highly variable as function of epicentral distance.

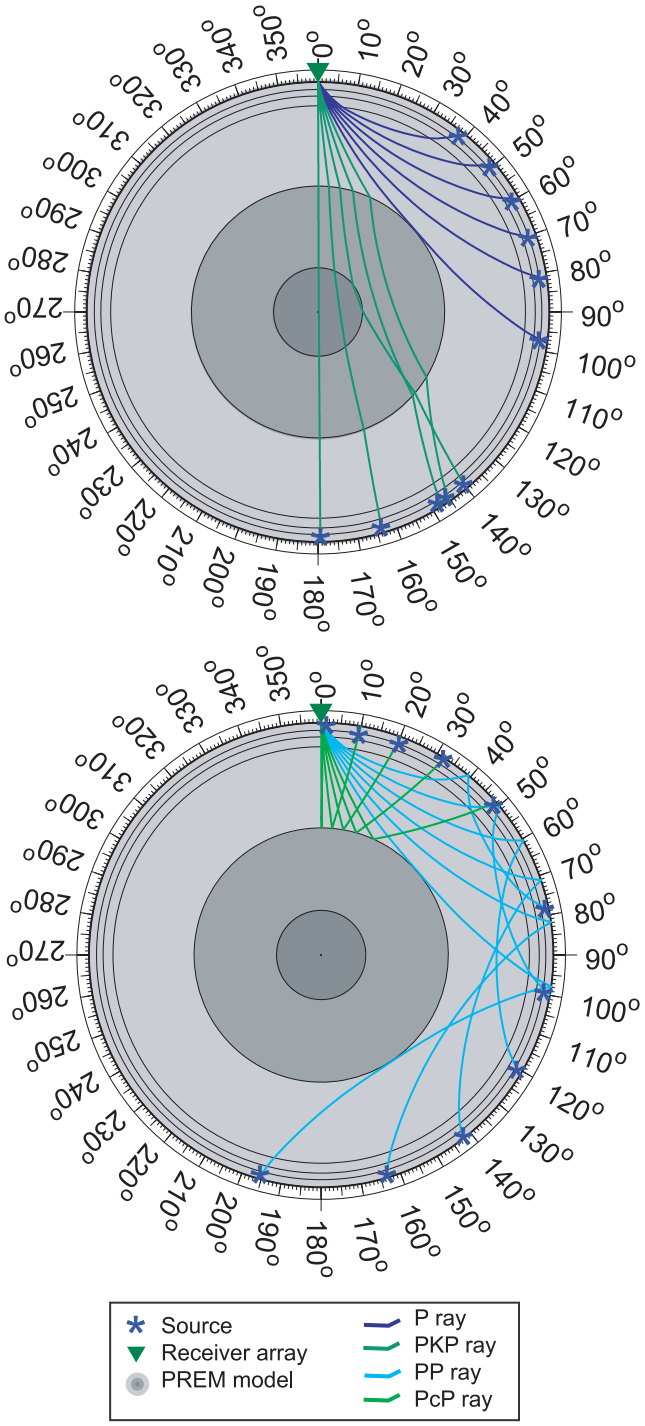

Figure A4. The source sampling required for lithospheric-scale SI, ray traced to a distribution of earthquakes at regional, teleseismic and global distances. The minimum distribution for *P* and *PKP* phases (up) and for *PP* and *PcP* phases (down).

APPENDIX B: FRESNEL ZONE

For a linear array and a subsurface with small lateral variations, a 3-D seismic-interferometry relation may be reduced to a 2-D version (eq. 4). For this 2-D version, the integration is over sources that lay in a vertical plane through the receiver positions (Fig. 3a). In practice, the source locations may be located outside this plane, as long as their contributions to the integral are in phase with the contribution

from sources in the plane. To find the region of acceptable source locations, we compute a proxy for the first Fresnel zone (Spetzler & Snieder 2004), considering a response retrieval between station $\mathbf{x}_\mathcal{A}$ and $\mathbf{x}_\mathcal{B}$.

$$\mathrm{d}t(\Delta,\theta) = \mathrm{d}t_{\mathcal{AB}}(\Delta,\theta=0) - \mathrm{d}t_{\mathcal{AB}}(\Delta,\theta) < \frac{1}{2f_{\max}}, \tag{B1}$$

where θ is the azimuth between the source and the array and $f_{\max}$ is the maximum frequency in the data. Here we assume a laterally invariant medium. Hence, all stationary phases must be located in the plane described by $(\Delta, \theta = 0)$. $\mathrm{d}t_{\mathcal{AB}} = t^{\mathrm{gh}}_\mathcal{B} - t^{\mathrm{dw}}_\mathcal{A}$ is the traveltime difference of a ghost reflection travelling from the source to receiver $\mathbf{x}_\mathcal{B}$ and a direct wave travelling from the source to receiver $\mathbf{x}_\mathcal{A}$. When ghost reflections are considered from reflectors which are much closer to the receiver array than to the sources, the following approximation may be used:

$$t^{\mathrm{gh}}_\mathcal{B}(\Delta,\theta=0) - t^{\mathrm{gh}}_\mathcal{B}(\Delta,\theta) \approx t^{\mathrm{dw}}_\mathcal{B}(\Delta,\theta=0) - t^{\mathrm{dw}}_\mathcal{B}(\Delta,\theta). \tag{B2}$$

Using approximation (B2), condition (B1) is simplified to

$$\mathrm{d}t(\Delta,\theta) = t^{\mathrm{dw}}_\mathcal{B}(\Delta,\theta=0) - t^{\mathrm{dw}}_\mathcal{A}(\Delta,\theta=0) - \left(t^{\mathrm{dw}}_\mathcal{B}(\Delta,\theta) - t^{\mathrm{dw}}_\mathcal{A}(\Delta,\theta)\right) < \frac{1}{2f_{\max}}. \tag{B3}$$

Since we only consider responses due to distant sources we may use eq. A6, with an additional $\cos(\theta)$ term to express the azimuthal dependence:

$$t^{\mathrm{dw}}_\mathcal{B}(\Delta,\theta) - t^{\mathrm{dw}}_\mathcal{A}(\Delta,\theta) = 2hp\cos(\theta). \tag{B4}$$

Combining eqs (B4) and (B3), we find

$$(1-\cos(\theta))2hp < \frac{1}{2f_{\max}}. \tag{B5}$$

Thus, we can express the width of the Fresnel zone in azimuth as

$$\theta_{\mathrm{FZ}} < 2\arccos\left(1 - \frac{1}{4h_{\max}pf_{\max}}\right). \tag{B6}$$

Fig. B1 depicts the azimuthal extent of the Fresnel zone as a function of epicentral distance, for the four different phases considered in this paper. These graphs are found by first computing the relationship between p and Δ through ray tracing (Fig. 1c) and subsequently using relation (B5), with for $h_{\max} = 20$ km and $f_{\max} = 1.5$ Hz. It is clear that the extent of the Fresnel zone is highly dependent on the phase of consideration. For example, the Fresnel zone for the *PcP* is very large, due to the small ray parameters involved, whereas for the *P* phase we may only include phases in a restricted azimuthal band.

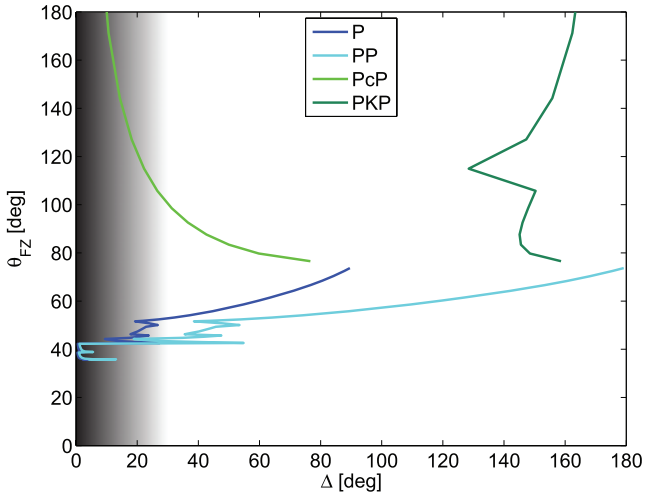

Figure B1. Extent of the Fresnel zone expressed in source-to-array azimuth (θ_{FZ}) as a function of epicentral distance (Δ) for four different *P*-wave phases. The grey shading depicts the distance range in which the approximations made for computing θ_{FZ} are increasingly invalid.

In Fig. 3(b) the extent of the Fresnel zone for $h_{\max} = 20$ km is plotted, on a global projection. Here only the direct-wave phases, *P* and *PKP*, are considered. The traveltime differences are computed using relation (B3) and the Fresnel zone is plotted in green. Dark green are locations for which the time difference is close to zero. Light green are locations for which the time difference is close to the threshold value (i.e. the right-hand side of relation B3). The function is evaluated for all source-array azimuths $[\theta = (0, 360^\circ)]$ and $\Delta = [0, 98^\circ]$ for the *P* phase and $\Delta = [117, 180^\circ]$ for the *PKP* phase. The traveltime differences are computed by ray tracing through the PREM model. When *P* or *PKP* is triplicated, the fastest arrival time is taken.

APPENDIX C: DECOMPOSTION AND ESTIMATION OF THE NEAR-SURFACE VELOCITIES

To apply acoustic SI relations (eqs 4 and 7), we need to find the compressional-wave component u_P from the recorded data. The data are recorded as $\mathbf{u}_m = (u_Z, u_N, u_E)$ (particle velocity in the vertical, north and east directions). After rotation, the responses are composed as $\mathbf{u}_s = (u_Z, u_R, u_T)$ (vertical, radial and transverse directions). In this appendix, the last step is described, that is, the decomposition into $\mathbf{u}_w = (u_P, u_{SV}, u_{SH})$ (compressional, shear inline and shear crossline).

The decomposition is performed by applying the inverse free-surface transfer matrix (Kennett 1991), with which $\mathbf{u}_w$ is expressed as function of $\mathbf{u}_s$, p, v_p^{ns} and v_s^{ns}. The last two variables, the near-surface compressional- and shear-wave velocity are initially unknown, but can be computed from the same decomposition relations, with two additional conditions and when assuming a 1-D and isotropic crust:

(i) the decomposition should give maximum amplitude on u_P and minimum amplitude on the other components for a *P*-wave arrival;

(ii) the decomposition should give maximum amplitude on u_{SV} and minimum on the other components for an *SV*-wave arrival.

Hence, as derived in Bostock & Rondenay (1999), the near-surface velocities can be expressed as functions of the p, the amplitude ratio u_R/u_Z for an incoming *P* wave and the amplitude ratio u_R/u_Z for an incoming *SV* wave. For estimating v_s^{ns}, clean teleseismic *P*-wave arrivals are required. For estimating v_p^{ns}, additionally clean teleseismic *S*-wave arrivals are required.

For five events, we estimated the v_s^{ns} values per station and subsequently averaged and smoothed the found values. For estimating v_p^{ns}, additionally two *S*-wave arrivals were used. Fig. C1 depicts the resulting near-surface velocity functions. The presence of a sedimentary basin $[x_1 = (3, 25)$ km] can easily be distinguished from hard-rock sites.

In Fig. C2, the u_Z and u_R components (dashed black) are shown at two receiver positions, for a time window around a *P*-phase arrival. Also, the results after decomposition, u_P and u_S, are shown in red. All used phase responses have relatively small incidence angles. Thus, generally, u_P is almost identical to u_Z, apart from

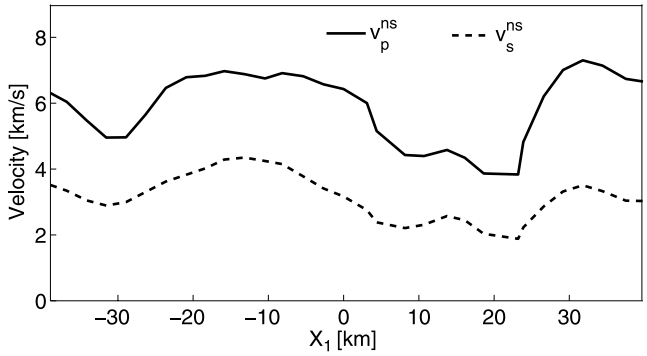

Figure C1. Estimated velocity model of the near surface.

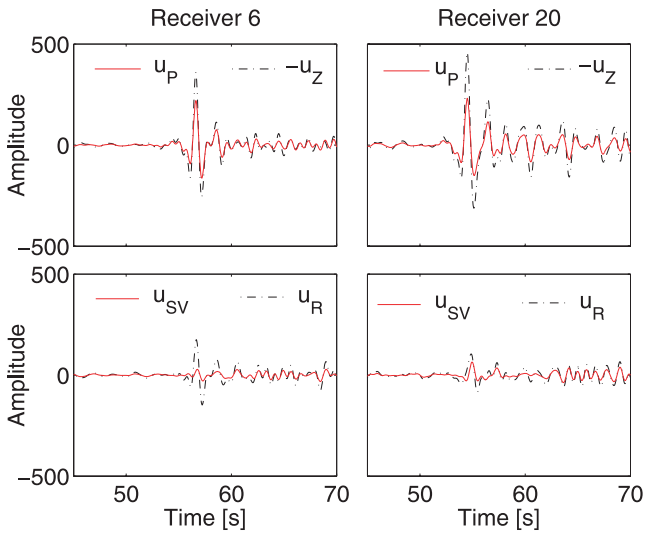

Figure C2. Particle velocity registration before (u_Z, u_R) and after (u_P, u_{SV}) decomposition for receiver 6 (left-hand side) and 20 (right-hand side). A time-window is shown which contains a *P*-phase arrival with $p = 0.057\ \mathrm{s\,km^{-1}}$.

the free surface amplification factor. The amplitudes on u_R and u_{SV} (conversions) are small with respect to the amplitudes on u_Z and u_P. The *SV*-wave component can be extracted quite well for a receiver at a hard-rock [Fig. C2 (left-hand side)], but u_{SV} remains polluted with near-surface scattering at a station on the sedimentary basin [Fig. C2 (right-hand side)]. This is already a clear indication that the subsurface is not horizontally layered below these stations, which is a condition for the used decomposition relations. Because of the large contamination on u_{SV}, applying a RF analysis would be a big challenge for a significant part of this data set. For *P*-wave interferometry, on the other hand, just using the Z-component might already give good results.

APPENDIX D: CORRELATION PANELS

In this appendix, the integrands (correlation panels) of eqs (4) and (7) are studied. This helps in understanding the modelling results as shown in Section 4. For the model as depicted in Fig. 4(b), transmission responses are modelled with the same ray parameter distribution as the Laramie phase distribution (Fig. 4a). The transmission responses are recorded by 31 receivers on the free surface. Subsequently, these transmission responses are used to estimate a retrieved response between receivers 16 and 8. Fig. D1 shows nine estimations of this response, for three different SI approaches (from left to right) and for three different data sets (from top to bottom). For each estimation, the different steps involved, are shown.

(i) A crosscorrelation of the transmission responses recorded at receivers 16 and 8. The crosscorrelation result is shown as a function of ray parameter (source position). With this visualization, the irregularity of the source distribution can easily be seen.

(ii) The result from integration over source positions. This boils down to stacking of the traces displayed in step 1, over ray parameter. For eq. (7) (right-hand panels) all the physical contributions are expected at positive times, thus the stacking result at negative times is muted.

(iii) For eq. (4) (left-hand and middle panels) also a third step is shown, which is an addition of the time-reversed acausal stack to the causal stack. For a perfect source distribution, this step may be left out, since the time-reversed acausal stack would be identical to the causal stack. For a biased irregular source distribution, the causal stack might be much more similar to the reflection response that the acausal stack, or vice versa. In this case, a better estimate is obtained when only one of the two is selected. For a more general irregular source distribution, as we have, the signal-to-noise ratio is improved by the addition of the time-reversed acausal stack to the causal stack.

Eq. (4) is applied without (left-hand panels) and with trace weighing (middle panels), based on Δp. In Fig. D1(right-hand panels) no trace weighing is applied and contributions from negative p's are time-reversed prior to stacking. Due to limited illumination, the complete integral in eq. (4) cannot be evaluated. In step 2 and 3 the retrieved response (solid red) is, where possible, compared with a reference reflection response (dotted black). In step 1 the largest feature is the event around $t = 0$ s, which is due to a crosscorrelation of direct waves. The crosscorrelation of direct waves would lead to the retrieval of a direct wave if we had sufficient illumination. Since we lack illumination by high ray parameters the event around $t = 0$ s does not include a stationary-phase region (Fresnel zone around $\partial_p \phi = 0$, where ϕ is the phase of an event and ∂_p denotes the derivative with respect to the ray parameter) and the only thing we are left with after stacking (step 2) are the spurious edge effects. The first two reflections (step 2 and 3) are retrieved with lower amplitude because only part of their stationary-phase region is covered and it is only sparsely sampled (check the events with corresponding times in step 1). The third reflection (Moho reflection) is generally retrieved well, but with a too low amplitude. To perfectly retrieve this Moho reflection at this offset (21 km), the illumination range would need to be extended to $p \approx 0.010\ \mathrm{s\,km^{-1}}$. Reflections and multiples at times later than the primary Moho reflection are almost perfectly retrieved. Their stationary-phase region is located in the teleseismic ray parameter-range and is therefore well sampled.

First, we consider the application of SI to synthetic single-phase responses (Fig. D1 top panels). For all the different SI approaches, the kinematic retrieval is comparable, but with trace weighing [Fig. D1(d)] the dynamic retrieval is clearly the best, at least for the events for which a large part of the stationary-phase region was captured (events at times later than 10 s).

Second, we consider the application of SI to single-phase responses, polluted with two source-side reverberations (middle panels). In all correlation panels, the addition of spurious cross terms (eq. 10) can clearly be seen. In Fig. D1(b) and (h), these cross terms are suppressed quite successfully. In Fig. D1(e), these cross terms are not suppressed well; large deviations from the reference

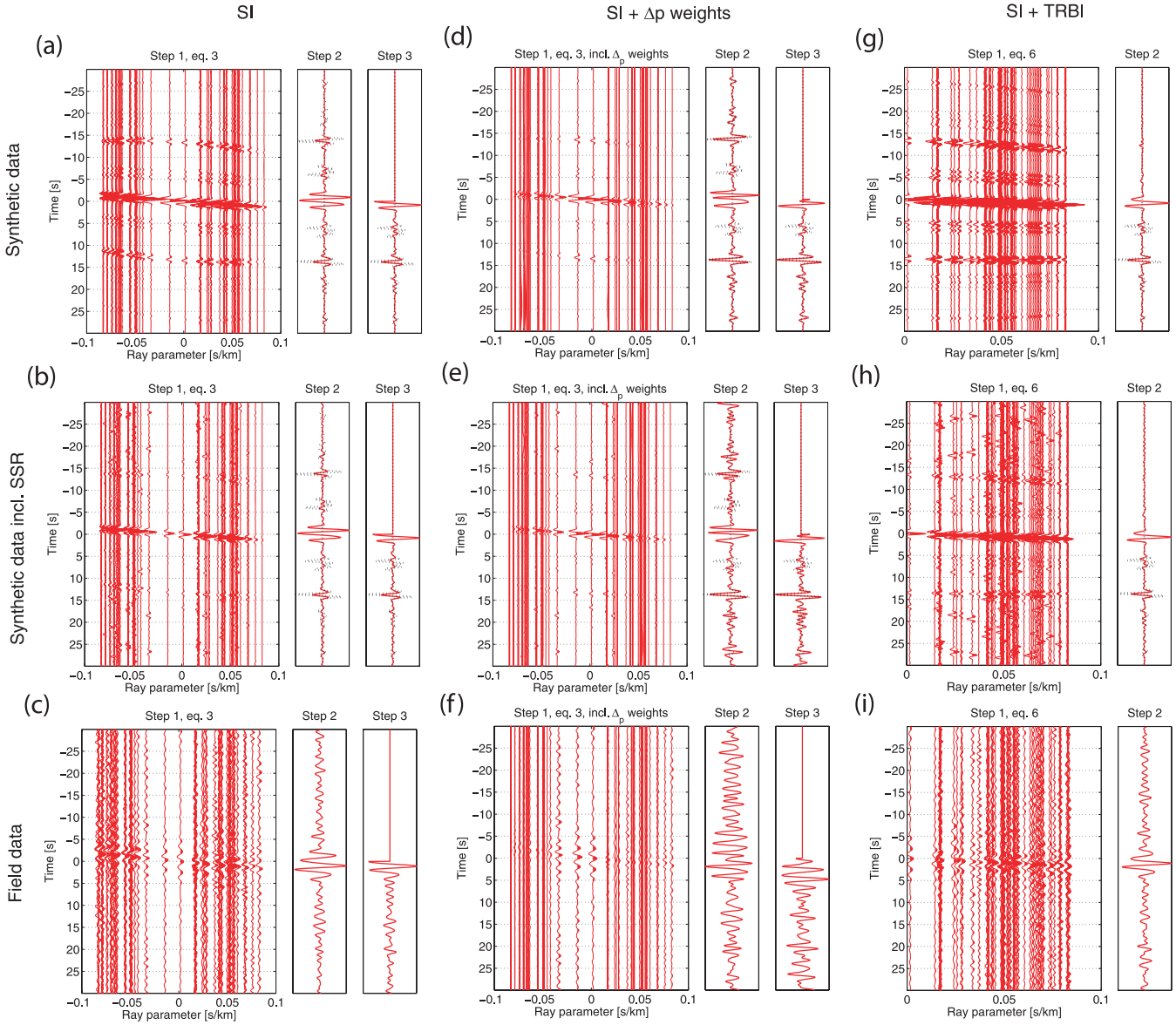

Figure D1. Visualization of the integrand (correlation panel) and integral (stack) of the seismic interferometric relations for $\mathbf{x}_{\mathcal{A}}$ and $\mathbf{x}_{\mathcal{B}}$ at station 16 and 8, respectively, for synthetic data (upper and middle panels) and the field data (lower panels). In the integrand displays, the traces are ordered as function of ray parameter. For the synthetic data, in step 2 and 3, a reference response is shown as a black dotted line. In (a)–(c) no adjustment is made for the irregular source distribution, in (d)–(f) every trace is weighted by its distance to the neighbouring traces and for (g)–(i) the traces caused by effective sources with negative ray parameters are time-reversed and displayed at positive ray parameter. (a), (d) and (g) are for isolated *P*-phase responses, whereas (b), (e) and (h) are for direct wave responses 'polluted' with two source-side reverberations (e.g. *pP* and *sP*) and (c), (f) and (i) are for the Laramie data from the field.

response can be noticed on the stack, for example, at $t = 26$ s. This happens because some cross terms are boosted due to the weighs applied.

Third, we consider the application of SI to phase responses detected at the Laramie array (lower panels). For the field data, it is much harder to distinguish events in the correlation panels (step 1). The actual subsurface is much more complicated than the model used for the synthetic data (Fig. 4b). Only the event caused by the crosscorrelation of direct waves can clearly be seen in Figs D1(c), (f) and (i). If this is not a clear linear event, errors were introduced during the pre-processing (e.g. a phase was misinterpreted). Of course it is not possible to compare the retrieved results (step 2 and step 3) with a reference response. Still it is clear that trace weighing [Fig. D1(f)] similarly as in Fig. D1(e), deteriorates the retrieval. Even more so for the field data, because trace weighing prejudices contributions from *PKP* phases here. *PKP* contains lower frequencies and more source-side reverberations than *P*, because it has seen more interfaces before it emerges on the lithosphere from below.

APPENDIX E: IMAGING STABILITY

In this appendix, we test how consistently different reflectors are imaged when varying subsets of phase responses are used. For the illumination range we consider in this paper [$p = (-0.08, 0.08)$ s km^{-1}] and the required sampling of $\mathrm{d}p = 0.0083$ s km^{-1} (Appendix A), a regular sampling of 21 clean phase responses would

suffice to retrieve good-quality reflection responses. However, for an irregular illumination with phase responses polluted with source-side reverberations (SSR), many more phase responses are required. In Section 4 it was shown that with 69 phase responses, the spurious contributions from SSR are significantly suppressed.

In the left-hand side of Fig. E1 subsets of the available phase responses are shown as ray parameter distributions. The subsets contain, from top to bottom, one-eighth, one-fourth, one-half and all of the available phase responses, respectively. The resulting images, for the different subsets, are shown on the right-hand side.

The shallow reflectors (see box 1 in Fig. E1) are consistently imaged for a varying amount of phase responses. Hence, the upper image [Fig. E1(a)] is already a good estimation of the shallow reflectivity, despite the fact that less phase responses are used than what the sampling condition prescribes. This is consistent with results from Draganov *et al.* (2006) and can be explained by the non-hyperbolic shape of undersampling artefacts. Due to this shape, the sampling artefacts are largely suppressed by the migration process. The reflectivity at larger depths, though, is heavily distorted by spurious reflectors which result from SSR. Spurious events due to SSR exhibit hyperbolic move-out in the shotgather and common-midpoint domain and are thus not suppressed by the migration. Since the contributions that result from SSR do not decay with depth, whereas actual reflections do, the distortions become more pronounced for larger depths. This explains why the shallow reflectors (see box 1 in Fig. E1) are consistent with a varying amount of phase responses, whereas deeper reflectors (box 2 and 3 in Fig. E1) only reveal themselves when larger numbers of phase responses are used, such that cross terms due to SSR (eq. 10) are increasingly suppressed. An example of the spurious contributions are highlighted in box 4. The apparent reflector in (a) changes phase in (b) and (c) and almost completely disappears in (d). Considering that still quite some spurious amplitudes disappear when we use 69 [Fig. E1(d)] instead of 35 [Fig. E1(c)] phase responses, even more than 69 would be required to remove all spurious amplitudes.

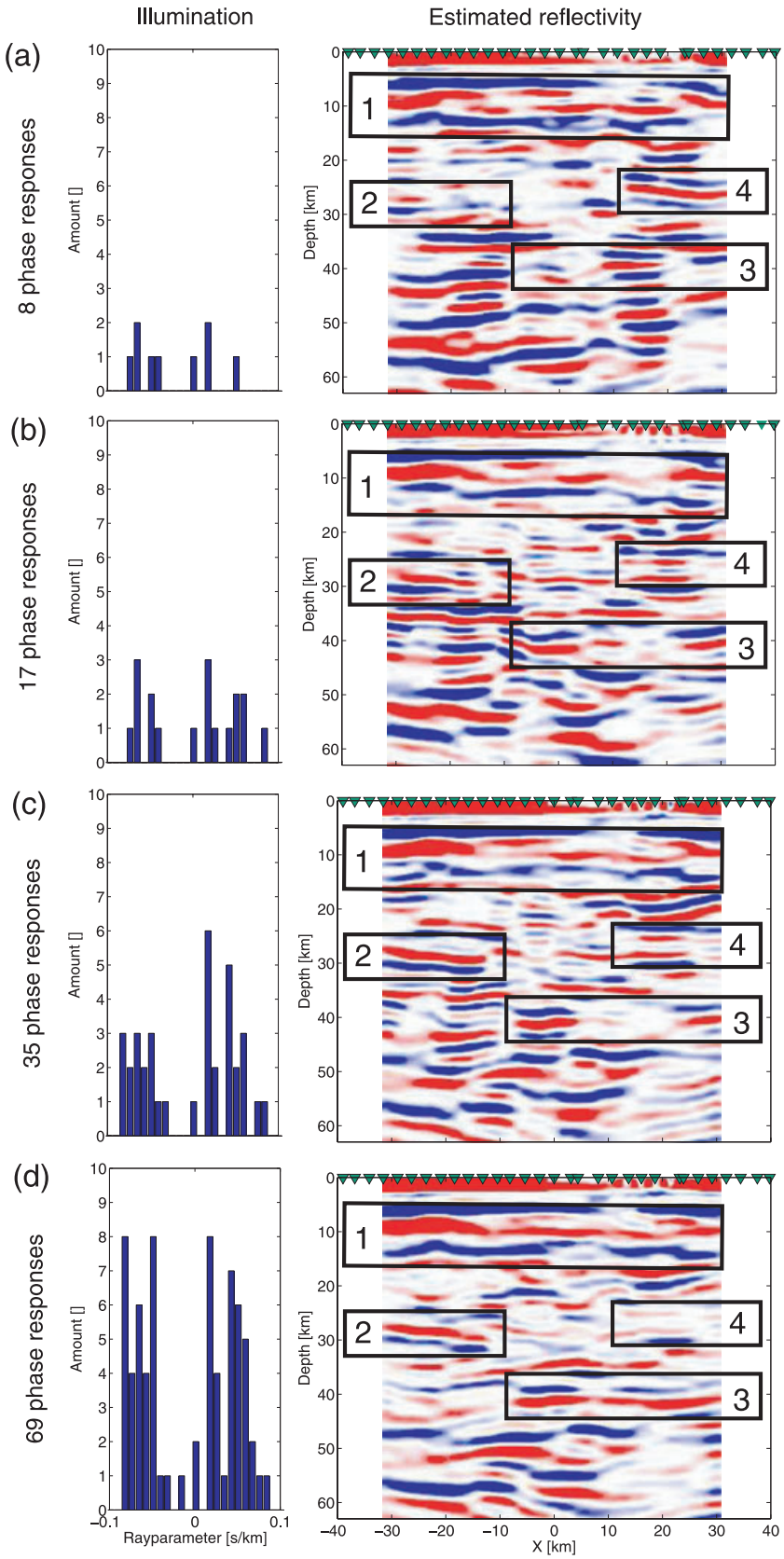

Figure E1. (Left-hand side) The ray parameter distrubution of a subset of phase responses and (right-hand side) the resulting image using only this subset of phase responses. The images are obtained using (a) 8, (b) 17, (c) 35 and (d) 69 phase responses.